



**Universität
Zürich^{UZH}**

A New Method for Simulating Gravitational Lensing Through Galaxy Clusters

Master Thesis in Astrophysics

Anna Katharina Rodriguez

Supervisor: Prof. Dr. Prasenjit Saha

Center for Theoretical Astrophysics and Cosmology
Institute for Computational Science

University of Zurich

December 2022

Abstract

In the presented work, gravitational lensing is investigated as a tool for studying the universe model. In a first step, the lensing equation is solved for an analytic potential. An algorithm for approximating a generic mass distribution is written. The main features of point mass distributions are captured. Additional noise is predicted in form of a fingerprint pattern. A simulation of a cosmological mass distribution is then analyzed and two galaxy clusters are cropped out of the simulation and reconstructed using a Fourier-Bessel series approach. The Fourier-Bessel series is determined for different numbers of Bessel roots, which determines the accuracy of the reconstruction. The gravitational potential is calculated from the reconstructions. The RMS for the error of the potential for galaxy cluster 1 are 8.45 picoradians for 50 Bessel roots and $3.31 \cdot 10^{-2}$ picoradians for 2238 Bessel roots. The specific values for galaxy cluster 2 are 7.15 picoradians for 50 Bessel roots and $3.26 \cdot 10^{-2}$ picoradians for 2238 Bessel roots. Subsequently, different spiral galaxies are used as source images to simulate gravitational lensing with the reconstruction of galaxy cluster 2 serving as gravitational lens. The distances between the image positions range from 3.91 microradians to 26.70 microradians. For a reconstruction with the maximum number of Bessel roots, time delays are predicted in a range from 5.31 days to 384.34 days. By inverting the equation for the time delay and using the fact that the angular diameter distances depend on the Hubble parameter of the current epoch, the Hubble parameter can be estimated. The Hubble tension is still an issue in the recent Λ CDM model of the universe. The approach of using gravitational lensing to determine the Hubble parameter of the current epoch provides a completely independent strategy. With the James Webb Space telescope, new data gets available and a huge potential is unlocked for which this tool can be helpful.

Contents

1	Introduction	3
1.1	Derivation of the Lens Equation	3
1.2	Distances	6
1.2.1	Comoving Distance	6
1.2.2	Angular Diameter Distance	6
1.3	Magnification	7
1.3.1	Hessian Matrix and Eigenvalues	7
1.3.2	Critical Curves and Caustics	8
1.4	Criterion for Multiple Image Formation	9
1.5	Resolution	10
1.6	Time Delay	11
2	Method	13
2.1	Analytic Potential	13
2.1.1	Code Structure and Output Images	13
2.2	Derivation of a Solution to Poisson Equation	14
2.2.1	Code Structure and Output Images	18
2.3	Time Delay and Hubble Parameter	21
2.3.1	Code Structure	22
2.4	Large Cosmological Simulation of Mass Distribution	23
2.4.1	Code	24
3	Results	25
3.1	Reconstruction of Mass Distribution	25
3.2	Gravitational Lensing of real Galaxies with reconstructed Clusters	30
3.2.1	Time Delay and of Image Distances	34
3.2.2	Estimation of the Hubble Parameter using a Noisy Potential	40
4	Discussion	42
4.1	Reconstruction of Mass Distributions	42
4.2	Gravitational Lensing of Real Galaxies with Reconstructed Clusters	44
4.3	Time Delays and Image Distances of Complete Reconstruction	45
5	Conclusion	47
6	Acknowledgements	49
A	Appendix	52
A.1	Error in the Mass Distribution	52
A.1.1	Total Mass Error	52
A.1.2	Fractional Mass Error	54
A.1.3	Error in the Potential	56
A.2	Time Delay	58
A.3	Image Distances	59

1 Introduction

As light travels through space, it interacts with nearby matter through gravity. Large masses such as a clusters of galaxies, bend the paths of nearby light by the gravitational field's attraction. This diffraction of light in a gravitational field was one of the first tests of Einstein's theory of general relativity (Mollerach and Roulet 2002). As early as 1920, multiple images due to the deflection of light deflection by stellar objects were postulated by Eddington (Eddington 1920). In order to find a quantitative explanation and make predictions, the lens equation was derived to quantitatively describe lensing effects due to stellar objects. In the following section the lens equation is derived.

1.1 Derivation of the Lens Equation

Throughout the derivation it is assumed that the gravitational potential ϕ is small compared to the speed of light c , i.e. $\frac{\phi}{c^2} \ll 1$. It is assumed that the velocity of the lens mass v is small compared to the cosmological rest frame, i.e. $v \ll c$ (Schneider, Ehlers, and Falco 1992). Because of these small perturbations, the Minkowski metric $ds^2 = dx^2 - c^2 dt^2$ locally changes to

$$ds^2 = \left(1 - \frac{2\phi}{c^2}\right) dx^2 - \left(1 + \frac{2\phi}{c^2}\right) c^2 dt^2. \quad (1)$$

Using the Taylor expansion $\sqrt{\frac{1+x}{1-x}} = 1 + x + O(x^2)$ and the fact that photons follow null geodesic, i.e. $ds = 0$ (Mollerach and Roulet 2002), Equation 1 can be transformed into

$$c' = \frac{dx}{dt} = c \left(1 + \frac{2\phi}{c^2}\right). \quad (2)$$

From Equation 2 it can be deduced that the light particles move with a modified speed c' . This speed can be used to determine the refractive index

$$n = \frac{c}{c'} = \left(1 - \frac{2\phi}{c^2}\right), \quad (3)$$

which is a result of the gravitational potential. Thus, the potential changes the refractive index and the light moves at a different speed. According to Fermat's principle, light takes an extremal path $x(l)$ from source to observer. Therefore, it is valid that

$$\delta \int n(x(l)) dl = 0. \quad (4)$$

New variables are introduced to describe gravitational lensing quantitatively. Figure 1 shows all relevant angles and distances, which are used to describe the source plane, the lens plane and the distances between source, lens and observer. A source at distance D_s from the observer emits light at an angle β to the observer. A cluster of galaxies at distance D_d from the observer deflects light by an angle of α , shifting the position of the light to an angle Θ with respect to the observer. It is possible that multiple extremal light paths exist and therefore multiple images can be observed. Since the distances D_d , D_s and D_{ds} are large compared to the size of the cluster, the problem can be treated in the thin lens approximation.

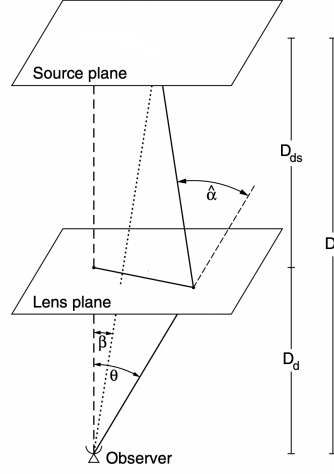


Figure 1: Illustration of the distances between observer, image plane and source plane. The angles β and Θ describe positions on the source and image plane. $\hat{\alpha}$ is the reduced deflection angle of the light (Schneider, Kochanek, and Wambsganss 2006).

Using Equation 4 and following the argumentation of Dodelson 2017, one obtains a deflection angle of

$$\alpha = -\frac{2}{c^2} \int \nabla_{\perp} \phi \, dl. \quad (5)$$

In the small angle approximation, the perpendicular distance can be described by ΘD_d , thus $\nabla_{\perp} = D_d^{-1} \nabla_{\Theta}$. It is convenient to define the reduced deflection angle $\alpha = \frac{D_s}{D_{ds}} \hat{\alpha}$, to make the deflection angle independent of distance. The deflection angle can be used to define a lensing potential Ψ

$$\begin{aligned} \nabla_{\Theta} \Psi &= \alpha \\ \Psi &= \frac{2}{c^2} \frac{D_{ds}}{D_d D_s} \int \phi \, dz \end{aligned} \quad (6)$$

Combining this equation with the Poisson equation $\nabla^2 \phi = 4\pi G \rho$ yields

$$\nabla_{\Theta}^2 \Psi = \frac{2}{c^2} \frac{D_{ds}}{D_d D_s} \int \nabla_{\Theta}^2 \phi \, dz = \frac{8\pi G}{c^2} \frac{D_d D_{ds}}{D_s} \Sigma, \quad (7)$$

where Σ is the density integrated along the line of sight. $\Sigma_c = \left(\frac{4\pi G}{c^2} \frac{D_d D_{ds}}{D_s} \right)^{-1}$ is the critical density that defines a criterion for the emergence of multiple images. Combining this with Equation 7 results in

$$\nabla_{\Theta}^2 \Psi = 2 \frac{\Sigma}{\Sigma_c} =: 2\kappa, \quad (8)$$

where convergence κ is introduced as $\kappa = \frac{\Sigma}{\Sigma_c}$.

Writing Equation 7 in terms of the deflection angle α yields

$$\nabla_{\Theta}\alpha = \frac{8\pi G}{c^2} \frac{D_d D_{ds}}{D_s} \Sigma. \quad (9)$$

For the relation between the angles, it holds that

$$\Theta_I = \beta + \alpha(\Theta_I) = \beta + \frac{D_{ds}}{D_s} \hat{\alpha}(\Theta_I), \quad (10)$$

where the reduced deflection angle $\hat{\alpha}$ is distance independent and completely constrained by the mass distribution of the galaxy cluster. Equation 10 is called the lens equation and is the central equation when dealing with light deflection by large mass distributions.

Integrating Equation 9 over all spatial coordinates results in

$$\alpha(\Theta) = \frac{4GM}{c^2} \frac{D_{ds}}{D_s D_d} \frac{\Theta}{|\Theta|^2}. \quad (11)$$

It is convenient to define the so-called Einstein angle

$$\Theta_E = \sqrt{\frac{D_{ds}}{D_s D_d} \frac{4GM}{c^2}}, \quad (12)$$

since it transforms the lens equation into a quadratic equation (Mollerach and Roulet 2002)

$$\Theta^2 - \beta\Theta - \Theta_E^2 = 0. \quad (13)$$

If the lens and source are perfectly aligned, $\beta = 0$, the observer sees a ring with the angular radius Θ_E .

In general, there are two solutions of Equation 13

$$\Theta_{\pm} = \frac{\beta}{2} \pm \Theta_E \sqrt{1 + \frac{\beta^2}{4\Theta_E^2}}. \quad (14)$$

Only for certain source positions, multiple images are generated.

It is possible to distinguish between microlensing and macrolensing (Narayan and Bartelmann 2008). In microlensing, the multiple images cannot be resolved because the observer is closer to the source than the images. It holds that $\Sigma < \Sigma_c$. An example of a microlensing system is the Sun which deflects light but not strongly enough to produce multiple images observable from Earth. In macrolensing, the bending of the light is strong enough so that the images can be resolved by the observer. It now holds that $\Sigma > \Sigma_c$.

1.2 Distances

Due to the expansion of the universe and the finite speed of light, there are several ways to measure distances in cosmology. (Hogg 2000) For the scope of this work, everything was calculated in angular diameter distances. The presented distance measures all depend on the Friedman-Robertson-Walker metric

$$ds^2 = c^2 dt^2 - a^2(t)[d\chi^2 + r^2(\chi)d\Omega], \quad (15)$$

which is the solution to Einstein's field equation assuming homogeneity and isotropy of space (Robertson 1936).

1.2.1 Comoving Distance

Consider a photon ($ds = 0$) moving radially toward an observer ($d\Omega = 0$) (Refregier 2021). Modifying the Friedman-Robertson-Walker metric accordingly yields

$$d\chi = \frac{c}{a(t)} dt. \quad (16)$$

Using the definition of the Hubble parameter $H = \frac{1}{a} \frac{da}{dt}$, this can be rewritten as:

$$d\chi = \frac{c}{a^2} \frac{da}{H(a)}. \quad (17)$$

Combining Equation 16 with Equation 17, yields

$$D_{AB}^{\text{cm}} = \int \frac{c}{a^2 H(a)} da, \quad (18)$$

where D_{AB}^{cm} is the comoving distance between point A and B .

1.2.2 Angular Diameter Distance

In small angle approximation, the perpendicular length of an object is equal to the product of its distance and the angle it spans (Refregier 2021). An object with physical transverse length L_{phys} is considered to have a fixed comoving radius χ ($d\chi = 0$) at a fixed time ($dt = 0$). Using again Friedman-Robertson-Walker metric, results in

$$\begin{aligned} L_{\text{phys}}^2 &= ds^2 = a^2 r(\chi)^2 \Delta\Theta^2 \\ L_{\text{phys}} &= ar(\chi)\Delta\Theta. \end{aligned} \quad (19)$$

Including the scale factor, gives the comoving transverse length $L_{\text{phys}} = aL_{\text{com}}$. Combining this with Equation 19 yields

$$\begin{aligned} L_{\text{com}} &= r(\chi)\Delta\Theta \\ r(\chi) &= \frac{L_{\text{com}}}{\Delta\Theta}. \end{aligned} \quad (20)$$

The physical angular diameter distance is then

$$D_{AB}^{\text{ang}} = ar(\chi) = \frac{L_{\text{phys}}}{\Delta\Theta}, \quad (21)$$

or written in terms of the comoving distance

$$D_{AB}^{\text{ang}} = \frac{D_{AB}^{\text{cm}}}{1+z}. \quad (22)$$

1.3 Magnification

If an image is gravitationally lensed, it can be magnified. More precisely, the surface brightness is preserved but the apparent solid angle of the source changes (Dodelson 2017). According to Mo, Van den Bosch, and White 2010, the magnification μ is measured by

$$\mu = \frac{\text{Image area}}{\text{Source area}}. \quad (23)$$

1.3.1 Hessian Matrix and Eigenvalues

The Hessian matrix H of the lensing potential Ψ equals

$$H = \begin{pmatrix} \Psi_{xx} & \Psi_{xy} \\ \Psi_{yx} & \Psi_{yy} \end{pmatrix} = \begin{pmatrix} \kappa + \gamma_x & \gamma_y \\ \gamma_y & \kappa - \gamma_x \end{pmatrix}, \quad (24)$$

where γ is a two-dimensional external shear (Wucknitz 2008). The convergence κ is the projected surface mass density Σ normalized by the critical density Σ_c . The resulting shear of the images is related to the projected foreground mass contrast inside an angular radius Θ (Vera C. 2022). The cosmic shear is the correlation between galaxy shapes, i.e. the systematic quadrupole alignment. This means that correlation in galaxy shapes, e.g. similar ellipticity, can be explained by the concept of cosmic shear. This results from the weak gravitational lensing of large-scale structures (Giblin et al. 2021).

In the regime discussed in this work, i.e. the regime of strong gravitational lensing effects, cosmic shear can be neglected. Alternatively, the impact of the cosmic shear could be induced by additional mass in the lens plane. This additional mass can be used to simulate the effects of cosmic shear on the system.

The inverse of the local magnification M can be expressed by the Hessian matrix of the lensing potential H (Courbin and Minniti 2002). The equation is

$$M^{-1} = 1 - H. \quad (25)$$

The scalar version of this equation is

$$\mu^{-1} = \det(1 - H) = (1 - \kappa)^2 - \gamma^2 = (1 - \kappa + \gamma)(1 - \kappa - \gamma), \quad (26)$$

with $\gamma^2 = \gamma_x^2 + \gamma_y^2$. The determinant of a matrix is the product of its eigenvalues, thus $1 - \kappa \pm \gamma$ are the eigenvalues of the matrix $1 - H$.

Considering a point mass, there always exists a minimum of the potential Ψ , which is a solution of the lens equation. This can be explained by the fact that when there is a minimum of Ψ , the gradient vanishes and so does the angle of deflection. Thus, the solution is $\Theta = \beta$.

The Hessian matrix has only positive eigenvalues for minima, giving $1 - \kappa \pm \gamma \geq 0$. The trace of μ^{-1} is positive for a minimum and since the trace is the sum of the eigenvalues, i.e. $2 - 2\kappa > 0 \implies \kappa \leq 1 \implies \gamma \leq 1 - \kappa \leq 1$. The convergence is non-negative, hence $0 < \mu^{-1} < 1$. Putting these things together yields

$\mu \geq \frac{1}{1 - \gamma^2} \geq 1$. Thus, images corresponding to a minimum are always magnified.

1.3.2 Critical Curves and Caustics

Critical curves are abstract curves in the sky that define the boundaries between regions of different image types, i.e. maxima, minima, or saddle points (Miranda 2007). As an observer moves or approaches, the regions adjust and move farther away so that a critical curve cannot be obtained. The Hessian matrix H given in Equation 24 has two eigenvalues, both positive for a minimum, both negative for a maximum and of mixed sign for a saddle point. At a critical curve, the sign of at least one eigenvalue changes.

Therefore, because of the continuity of H , at least one eigenvalue must vanish. The Hessian matrix is the inverse of the magnification. Consequently, the magnification on a critical curve becomes infinite (Mollerach and Roulet 2002).

Caustics are critical curves mapped onto the source plane via the lens equation and are therefore real places that could theoretically be visited. Practically, however, they are not, since the universe is expanding.

1.4 Criterion for Multiple Image Formation

The goal now is to find a condition for the formation of multiple images. The basis for the derivation of a criterion for the formation of multiple images is a theorem formulated by Burke.

Theorem 1 (*Burke's theorem*): *Any smooth bounded gravitational lens produces an odd number of images. A gravitational lens will always produce at least one image with positive parity and additional images which will appear in pairs with $\mu^{-1} > 0$ for one and $\mu^{-1} < 0$ for the other (Burke 1981).*

The following more formal proof follows the argumentation of Subramanian and Cowling 1986.

Theorem 2 : *Multiple imaging by a smooth bounded gravitational lens is possible if and only if there exists a point on the image plane (Θ_x, Θ_y) , where $\mu^{-1} = \det(1 - H)$, is negative.*

Proof: According to Burke's theorem the minimal number of multiple images is three. Two of the images have positive parity and the third has negative parity, which means that locally $\mu^{-1} < 0$. Hence, the existence of multiple images implies a point in the image plane, where $\mu^{-1} < 0$.

Suppose there is a point (Θ_1, Θ_2) with $\mu^{-1} < 0$, it can be related to a point in the source plane, e.g. (β_1, β_2) , via the lens equation. Now, if the source is located at (β_1, β_2) , an image with $\mu^{-1} < 0$ is formed at (Θ_1, Θ_2) . According to Burke's theorem, this cannot be the only image, so multiple images can occur. \square

Theorem 3 *If there exists a point Q on the lens, where the projected surface density $\Sigma(Q)$ exceeds Σ_c , with $\Sigma_c = \left(\frac{c^2}{4GD\pi}\right)$, then the lens is capable of producing multiple images.*

Proof: If at a point Q in the lens plane $\Sigma > \Sigma_c$, then $\kappa > 1$ and

$B := \frac{1}{2}\text{tr}(1 - H) = 1 - \kappa < 0$ at Q . An arbitrary curve C , which starts at Q and goes to infinity is considered. B is a continuous function, because the trace is a continuous function. At infinity, B is equal to 1 because there is no mass at infinity. Therefore, it must become zero somewhere on C , since it is negative at Q . This is true for any C , so there is a closed curve C' enclosing Q on which $B = 0$ and $\kappa = 1$. On the curve C' it holds that $\mu^{-1} = \det(1 - H) = (1 - \kappa)^2 - \gamma^2 = -\gamma^2 \leq 0$. There are two cases to distinguish: either $\mu^{-1} = 0$ on the whole curve C' , or $\mu^{-1} < 0$ in at least one point and then multiple images are possible due to Theorem 2. Thus, only the first case needs to be shown. Whitney (1995) has shown that any map can be approximated arbitrarily close by a map which has $\mu^{-1} \neq 0$ at points where $\kappa = 1$ (Whitney 1995). The physical solution would be to have an arbitrarily small smooth mass perturbation in a small region outside C' that leaves $\kappa = 1$ but gives μ^{-1} a value less than zero. Since such small perturbations will most likely always exist in real galaxies, this case can be ruled out as unrealistic. \square

1.5 Resolution

The angular resolution provides information about the ability to detect small details. More precisely, it indicates the smallest angle that can be resolved by a telescope or other optical instrument. For light passing through an aperture, the observed diffraction pattern is inversely proportional to the size of the aperture, i.e. the diffraction pattern is the Fourier transform of the aperture (Hecht 2016). In the case of a circular aperture, the diffraction pattern is given by a first kind Bessel function. The pattern is called airy pattern. It consists of a bright central area and a series of concentric rings around this. The size of the central bright spot is

$$d = 3.83 \frac{\lambda z}{2\pi b}, \quad (27)$$

with the wavelength of the light λ , the radius of the aperture b and the vertical distance to the aperture z . This leads to the Rayleigh criterion for circular apertures

$$\sin(\Theta) = 1.22 \frac{\lambda}{D}, \quad (28)$$

with the minimal resolvable angle Θ , the wavelength λ and the diameter D . The criterion was first derived in 1888 (Lord Rayleigh 1888). It applies to systems with one primary mirror. Since telescopes and other measuring instruments often have multiple mirrors, it is assumed that the following criterion applies to systems with multiple mirrors:

$$\sin(\Theta) \approx \frac{\lambda}{D}. \quad (29)$$

Figure 2 shows a sketch of a telescope setup, where the gray box on the right corresponds to a charge-coupled device (CCD) sensor (Mercieca 2016).

The sensor consists of small boxes into which photons fall. The size of these boxes determines the size of the pixels P_s . From the geometry of the structure, see Figure 2, one can deduce

$$\Theta \approx \tan(\Theta) = \frac{P_s}{F_L}, \quad (30)$$

with F_L being the focal length of the telescope. In the equation, the small angle approximation is used. The focal length of the telescope is given in $[F_L] = 1 \text{ mm}$. The pixel size is given in $[P_s] = 1 \text{ }\mu\text{m}$. From Equation 30, the unit $[\Theta] = \text{radians/pixel}$ is deduced for the minimal resolvable angle Θ .

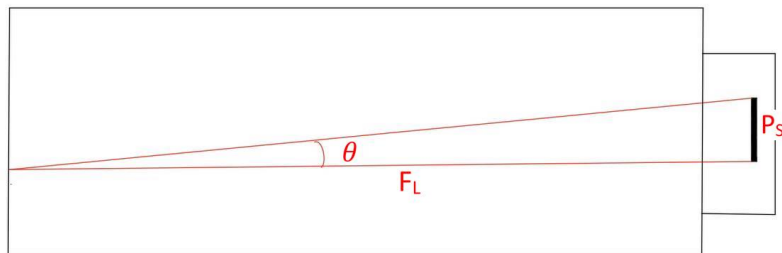


Figure 2: Schematic of a telescope setup, showing the principle of unit conversion from radians to pixel. The figure is a modified and adapted version of the original version (Mercieca 2016).

1.6 Time Delay

When light travels along different paths, the light travel time is not necessarily equal along all paths. The difference in arrival time between images of a multiply imaged source is called time delay.

There are two different reasons for time delay when light travels along different paths (Narayan and Bartelmann 2008). Geometrical time delay is due to the extended path of light around the lens. The gravitational time delay is caused by the increased refractive index introduced by the gravitational lens, resulting in a decreased speed of light. The total time delay is the sum of the geometrical and gravitational time delays (Courbin and Minniti 2002).

$$t = t_{geom} + t_{gravit} = \frac{1 + z_d}{c} \frac{D_d D_s}{D_{ds}} \left[\frac{1}{2} (\Theta - \beta)^2 - \frac{D_{ds}}{D_s} \Psi(\Theta) \right]. \quad (31)$$

Equation 31 provides a theoretical prediction of the time delay, which is completely determined by the image positions Θ , the source positions β , the gravitational potential Ψ and the distances between observer, source plane and image plane, i.e. D_d , D_s and D_{ds} . In addition, the redshift of the lens z_d affects the time delay. The Hubble parameter of the current epoch (H_0) is implicit in the formula, since the angular diameter distances depend on it. It can be factored out of the distances, so no assumptions are made about H_0 . The theoretical prediction of the time delay can be compared with a corresponding measurement.

Time delays can only be measured if the source under investigation contains a varying light source, e.g. a quasar or blazar. In this case, the difference in arrival time can be measured. The comparison between the measured time delay and the theoretical values allows the determination of H_0 .

The approach to determine H_0 is motivated by the Hubble tension, which is a statistical disagreement between different predictions of H_0 . On one side are the predictions of the

Λ CDM model for the early universe and on the other side are the model-independent estimates from local distances and redshift measurements (Di Valentino et al. 2021). The determination of H_0 by gravitational lensing is an alternative approach and represents an opportunity to find a more precise value for the parameter. Because of the many sources of uncertainty, predictions from gravitational lensing have not yet been able to provide a consistent value. However, with the James Webb Space Telescope (JWST), many more lensing systems are being discovered and studied, making it more likely to make accurate predictions from gravitational lensing using the time delay method.

2 Method

The following section contains a documentation of the working process. All files containing the codes can be found in: DOI:10.5281/zenodo.6793513.

2.1 Analytic Potential

In a first step, image transformations of galaxies in the Hubble Deep Field are studied using analytic potentials. The lens equation, Equation 10, is used to calculate the new image positions including a deflection angle. The reduced deflection angle is determined using the two-dimensional gradient of the analytic potential

$$\Psi = \pm C \cdot \ln(1 + x^2 + qx^2). \quad (32)$$

The combination of Equation 6 and Equation 32 gives

$$\alpha_x = \pm C \cdot \frac{2x}{1 + x^2 + qy^2}, \alpha_y = \pm C \cdot \frac{2qy}{1 + x^2 + qy^2}. \quad (33)$$

The distances are calculated as angular diameter distances, see Equation 22.

2.1.1 Code Structure and Output Images

This section corresponds to the file `AnalyticPotential.py`. An image of Hubble Deep Field is uploaded. The resolution is 1280×1280 pixels. Different galaxies are cropped from the Hubble Deep Field image and put at different redshifts, i.e.

$z_1 = 9, z_2 = 1.8, z_3 = 2, z_4 = 5, z_5 = 2.1, z_6 = 7, z_7 = 6$. The angular diameter distances between observer, source and fictive lens are calculated by Equation 22. The transformed images can be calculated using the lens equation (Equation 10). The deflection angles are determined by Equation 33, using the constants $C = 20000$ and $q = 0.8$. A spline function is used to interpolate the source plane and assign float values to the source positions. Figure 3 shows the cropped images and Figure 4 the corresponding lensed images.

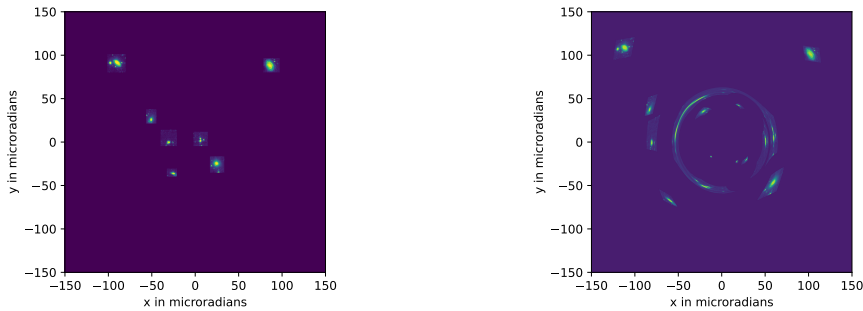


Figure 3: Galaxies cut out of Hubble Deep Field
Figure 4: Images lensed by the analytic potential

2.2 Derivation of a Solution to Poisson Equation

The next goal is to determine the gravitational potential numerically. It is possible to use an arbitrary mass distribution and solve the two-dimensional Poisson equation.

When gravitational lensing is considered on cosmological scales, the distances between the source, the lensing cluster and the observer are many orders of magnitude greater than the height of the cluster itself; therefore, the problem can therefore be considered to be two-dimensional.

One attempt to find the potential is to use Bessel functions. Bessel functions are the solution $y(x)$ of the equation

$$x^2 \frac{d^2 y}{dx^2} + x \frac{dy}{dx} + (x^2 - \alpha^2)y = 0, \quad (34)$$

for $\alpha \in \mathbb{C}$ (Andrews 1999). If α is an integer or a half-integer, the corresponding Bessel functions are the eigenfunctions of the two-dimensional Laplace equation in cylindrical coordinates. The strategy is now is to expand the potential Ψ in a Fourier-Bessel series in angular coordinates and Bessel functions in radial coordinates. The Fourier-Bessel series is

$$\sum_{mn} c_{mn} J_m(\alpha_{mn} r) e^{imr}, \quad (35)$$

where J_m is the m^{th} first-order Bessel function. α_{mn} is the n^{th} roots of the m^{th} Bessel function (Magnus, Oberhettinger, and Soni 1966). r is a spatial coordinate. The approach now is to consider all zeros of the Bessel functions up to a spatial threshold.

The two-dimensional Poisson equation is

$$\Delta \Psi(r, \Theta) = 2\kappa(r, \Theta), \quad (36)$$

where Ψ is the gravitational potential and κ is the convergence, which can be treated as a two-dimensional density (Schneider, Kochanek, and Wambsganss 2006). The gravitational constant as well as other constants are absorbed in the convergence.

One approach to solving the two-dimensional Poisson equation is to find eigenfunctions ϕ_{mn} with eigenvalues λ_{mn} of the two-dimensional Laplace operator. The solution is written as a superposition of these eigenfunctions, i.e. $\Psi = \sum_{mn} \phi_{mn}$. Then

$$\begin{aligned} \Delta \phi_{mn} &= \lambda_{mn}^2 \phi_{mn}, \\ \partial_r^2 \phi_{mn} + \frac{1}{r} \partial_r \phi_{mn} + \frac{1}{r^2} \partial_\Theta^2 \phi_{mn} - \lambda_{mn}^2 \phi_{mn} &= 0. \end{aligned} \quad (37)$$

A separation approach can be used to solve the problem, i.e.

$\phi_{mn} = R_m(r) \cdot v_n(\Theta)$. Combining this approach with Equation 37, yields

$$\begin{aligned} \ddot{R}_m(r) v_n(\Theta) + \frac{1}{r} \dot{R}_m(r) v_n(\Theta) + \frac{1}{r^2} R_m(r) \ddot{v}_n(\Theta) - \lambda_{mn}^2 R_m(r) v_n(\Theta) &= 0 \\ \frac{\ddot{R}_m(r)}{R_m(r)} + \frac{1}{r} \frac{\dot{R}_m(r)}{R_m(r)} + \frac{1}{r^2} \frac{\ddot{v}_n(\Theta)}{v_n(\Theta)} - \lambda_{mn}^2 &= 0. \end{aligned} \quad (38)$$

The equation must be fulfilled for any Θ and r and is divided into two parts, one of which depends only on r and the other only on Θ . Both parts must be constant for the equation to hold for any value of r and Θ . So it is possible to set

$$\frac{\ddot{v}_n(\Theta)}{v_n(\Theta)} = -m^2. \quad (39)$$

The general solution to this differential equation is

$$v_n(\Theta) = \sum_m (a_{mn} \sin(m\Theta) + b_{mn} \cos(m\Theta)), \quad (40)$$

where v_n is a function of Θ and thus single-valued. This means that m must be an integer, since $\sin(m\Theta)$ and $\cos(m\Theta)$ are linearly independent only when m is an integer. Plugging m into Equation 38 yields

$$\ddot{R}(r) + \frac{1}{r} \dot{R}(r) + \left(\frac{m^2}{r^2} - \lambda_{mn}^2 \right) R(r) = 0. \quad (41)$$

Substituting $\rho = \lambda_{mn}r$, Bessel's equation is obtained:

$$\frac{d^2 R}{d\rho^2} + \frac{1}{\rho} \frac{dR}{d\rho} + \left(1 - \frac{m^2}{\rho^2} \right) R = 0. \quad (42)$$

Since m must be an integer, the solution of Equation 42 are Bessel functions of the first kind, i.e. $R_m = J_m(\lambda_{mn}r)$. The entire density distribution is contained in a disk, and it is therefore reasonable to choose the boundary condition, such that the functions vanish at a certain radius r_{\max} . This constrains the Bessel functions to vanish at this radius. The argument of the Bessel function must therefore fulfill the following condition:

$$J_m(\lambda_{mn}r) = J_m \left(\frac{r}{r_{\max}} \alpha_{mn} \right). \quad (43)$$

This directly implies that

$$\lambda_{mn} = \frac{\alpha_{mn}}{r_{\max}}. \quad (44)$$

Thus, the total solution of the two-dimensional Poisson equation is

$$\Psi = \sum_{mn} (a_m \sin(m\Theta) + b_m \cos(m\Theta)) \cdot J_m \left(\frac{r}{r_{\max}} \alpha_{mn} \right). \quad (45)$$

The Fourier-Bessel series forms a complete basis. This result justifies the superposition and makes it a general approach.

The combination of all results leads to

$$\Delta \Psi = \sum_{mn} \Delta \phi_{mn} = \sum_{mn} \lambda_{mn}^2 \phi_{mn} = 2\kappa = 2 \sum_{mn} \kappa_{mn}, \quad (46)$$

hence there exists a correlation

$$\phi_{mn} = \frac{2}{\lambda_{mn}^2} \kappa_{mn}. \quad (47)$$

Inserting Equation 44 into Equation 47 gives

$$\phi_{mn} = 2 \left(\frac{r_{\max}}{\alpha_{mn}} \right)^2 \kappa_{mn}. \quad (48)$$

The next step is to find the coefficients of the series. For this purpose, the orthogonality of differently scaled Bessel functions can be used. Since the basis functions are orthogonal but not orthonormal, a normalization constant must be implemented. For first-order Bessel functions it is generally true that

$$\int_0^1 r J_m(r\alpha_{mn}) J_m(r\alpha_{mk}) dr = \frac{\delta_{nk}}{2} [J_{m+1}(\alpha_{mn})]^2, \quad (49)$$

see Guan, Lai, and Wei 2001. When the maximum radius is introduced this conditions changes to

$$\int_0^{r_{\max}} r J_m(r\alpha_{mn}) J_m(r\alpha_{mk}) dr = \frac{\delta_{nk}}{2} r_{\max}^2 [J_{m+1}(\alpha_{mn})]^2 \quad (50)$$

The basis functions of the potential are

$$\begin{aligned} \cos(m\phi) J_m(\alpha_{mn} r), \\ \sin(m\phi) J_m(\alpha_{mn} r) \end{aligned} \quad (51)$$

for $m \geq 0$. If two basis functions are multiplied and integrated over angle and radius, two different integrals are obtained:

$$\begin{aligned} \int_0^{2\pi} d\phi \cos^2(m\phi) \int_0^{r_{\max}} dr r J_m(\alpha_{mn} r) J_m(\alpha_{mk} r) r \\ = \int_0^{2\pi} d\phi \sin^2(m\phi) \int_0^{r_{\max}} dr r J_m(\alpha_{mn} r) J_m(\alpha_{mk} r) r \end{aligned} \quad (52)$$

and

$$\int_0^{2\pi} d\phi \cos(m\phi) \sin(m\phi) \int_0^{r_{\max}} dr r J_m(\alpha_{mn} r) J_m(\alpha_{mk} r) r, \quad (53)$$

where Equation 50 can be used for the Bessel function part of the integral. For the trigonometric integral, the following applies:

$$\begin{aligned} \int_0^{2\pi} \sin^2(m\phi) = \int_0^{2\pi} \cos^2(m\phi) = \pi \\ \int_0^{2\pi} \sin(m\phi) \cos(m\phi) = 0 \end{aligned} \quad (54)$$

Combining Equation 50 with Equation 54, the normalization constant is obtained

$$N_{mn} = r_{\max}^2 \frac{\pi}{2} J_{m+1}(\alpha_{mn})^2 \quad (55)$$

for $m > 0$. In the special case of $m = 0$, the basis function containing a sinus vanishes and $\cos(m\Theta) = 1$ which gives a basis function of the type

$$J_{mn}(\alpha_{mn} r). \quad (56)$$

Integration over ϕ results in a factor 2π . Combining this with Equation 50 yields

$$N_{0n} = r_{\max}^2 \pi J_1(\alpha_{0n}). \quad (57)$$

The coefficients are then determined using

$$\begin{aligned} a_m &= \frac{1}{N_{mn}} \int_0^{2\pi} d\phi \int_0^{r_{\max}} dr r J_m \left(\alpha_{mn} \frac{r}{r_{\max}} \right) \kappa(r, \phi) \sin(m\phi) \\ b_m &= \frac{1}{N_{mn}} \int_0^{2\pi} d\phi \int_0^{r_{\max}} dr r J_m \left(\alpha_{mn} \frac{r}{r_{\max}} \right) \kappa(r, \phi) \cos(m\phi). \end{aligned} \quad (58)$$

2.2.1 Code Structure and Output Images

This section corresponds to the files `Poissonequation.py` and `Bessel.py`. First, the maximum observable orthogonal radius, i.e. the angle observed by a fictitious telescope, must be determined. In a second step, the resolution can be chosen. A maximum radius of $r_{\max} = 150$ microradians and a resolution of $R = 250 \times 250$ pixels are chosen, creating a quadratic grid of length $2r_{\max}$ with a pixel size of $\frac{2r_{\max}}{R}$. A mass distribution is generated by assigning a value to each pixel, as shown in Figure 7.

Intermezzo: In a separate code the roots of the first-order Bessel functions are determined. The zeros of the Bessel function are determined numerically using the approach that the n^{th} zero of the m^{th} Bessel function resides within the interval

$$\begin{aligned} J_{0n} &= [\pi \cdot (n + 0.75), \pi \cdot (n + 0.8)] \\ J_{mn} &= [\alpha_{m-1n} + 1, \alpha_{m-1n} + \frac{\pi}{2}]. \end{aligned} \tag{59}$$

Each interval is divided in half multiple times and a bisection algorithm is used to find a possible zero. After the first root is found, the higher order roots can be found iteratively. The determined Bessel roots within r_{\max} for the first 70 Bessel functions are shown in Figure 5. There are no gaps in the ordering of the zeros, which confirms the assumption about the intervals given in Equation 59.

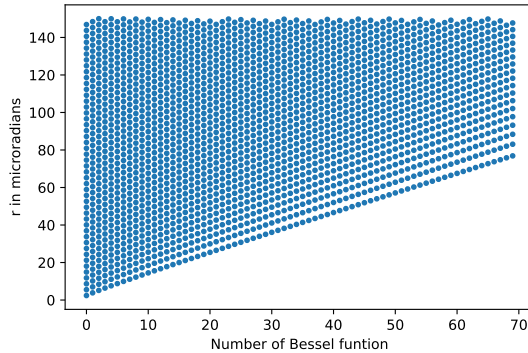


Figure 5: The determined zeros of the first fifty first-order Bessel functions

All roots and the corresponding indices are appended as a tuple to a list. Finally, the list is sorted so that the roots ascend in order. The list can be imported back into the main code.

After the roots of the Bessel functions have been found, the basis functions are determined. The first eight basis functions of the Fourier-Bessel series are shown in Figure 6. Equation 58 is used to calculate the coefficients of the Fourier-Bessel series. The normalization constants are determined according to Equation 57 and Equation 55. The integrals can be approximated assuming that the value of the integrand is constant for each pixel. This value is multiplied by the area of the pixel, i.e. $\frac{4r_{\max}^2}{R^2}$. Summing over all pixels gives the value of the entire integral. After the coefficients are found, the full

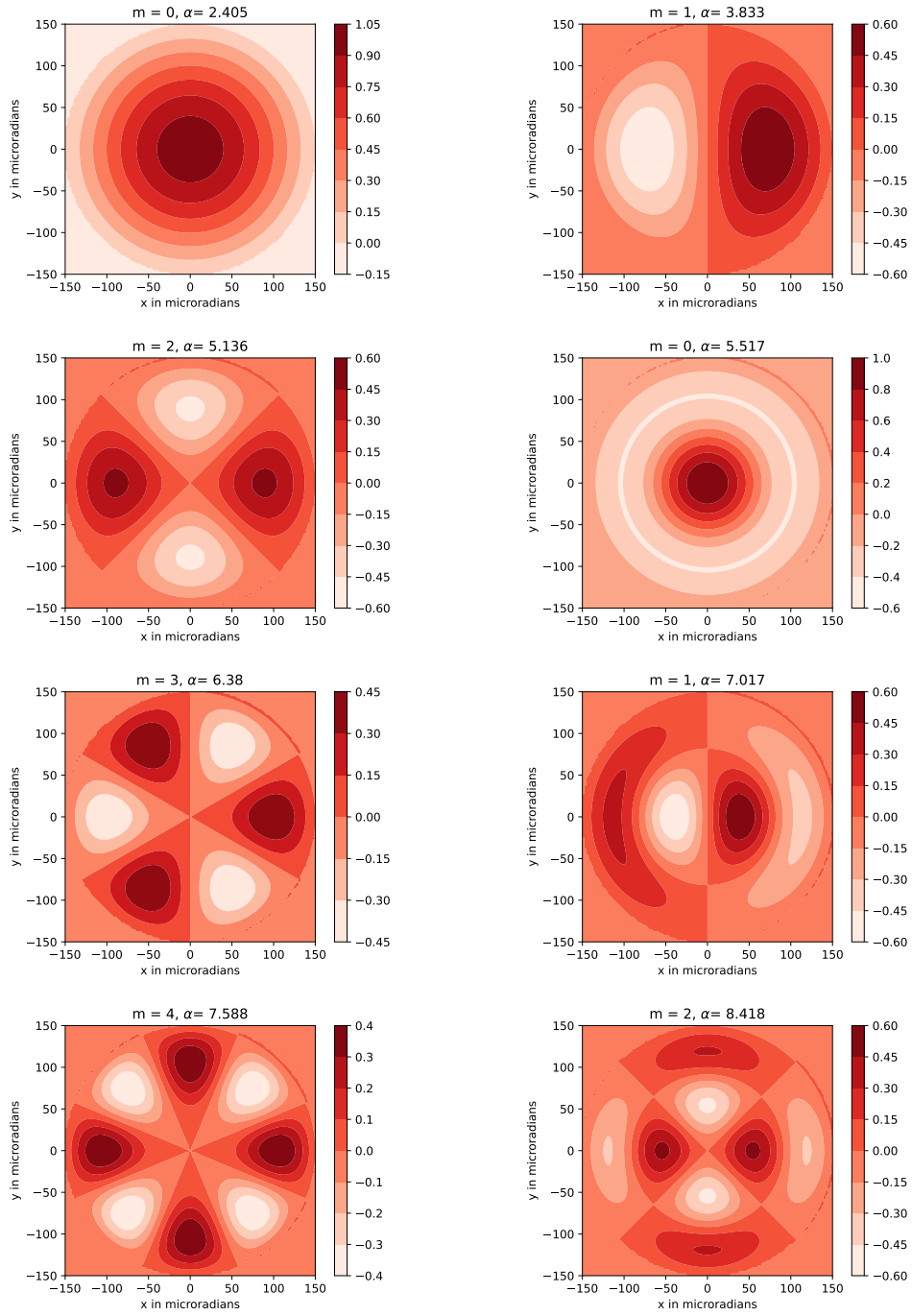


Figure 6: Basis functions of the Fourier-Bessel series for different m and α

Fourier-Bessel series is determined using Equation 45. The reconstructed mass distribution is shown in Figure 8. According to Equation 48 an additional factor of $2 \left(\frac{r_{\max}}{\alpha_{mn}} \right)^2$ must be introduced in order to obtain the gravitational potential shown in Figure 9.

In a next step, the derivative of the Fourier-Bessel series is determined analytically, but as a function of the coefficients of the Fourier-Bessel series. Using the numerically determined coefficients, an approximation of the derivatives is found.

The Fourier-Bessel series is written as a function of radius and angle, so that first the derivatives are considered according to radius and angle. In a next step, the gradients are determined with respect to the Cartesian coordinates by using the following relations for the coordinate transformation:

$$\begin{aligned} X_{\text{grad}} &= r_{\text{grad}} \cdot X/r - \phi_{\text{grad}} \cdot Y/r \\ Y_{\text{grad}} &= r_{\text{grad}} \cdot Y/r + \phi_{\text{grad}} \cdot X/r. \end{aligned} \quad (60)$$

A quiver plot of the gradient in terms of Cartesian coordinates is shown in Figure 10.

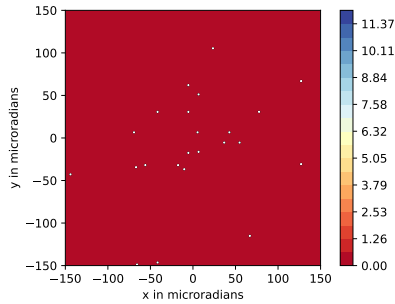


Figure 7: Point mass distribution

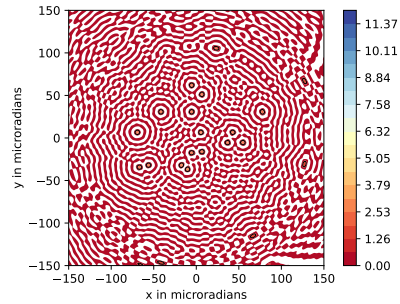


Figure 8: Point mass reconstruction

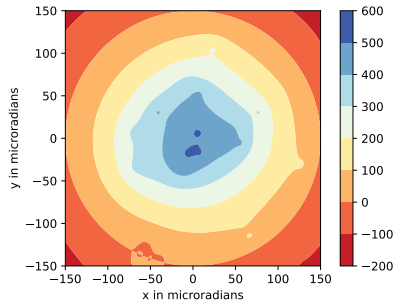


Figure 9: Gravitational potential

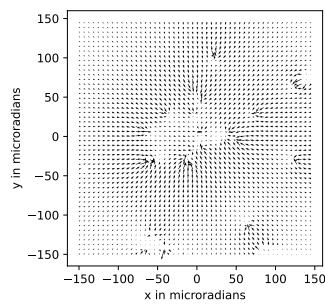


Figure 10: Reduced deflection angle

In analogy to Section 2.1.1, where an analytic potential was used, the image positions are determined using the lens equation.

2.3 Time Delay and Hubble Parameter

To determine the total time delay resulting from the geometrical and gravitational time delay, Equation 31 is used. An arrival time surface is calculated for each lensing event. The lens equation is fulfilled for the condition $\nabla \tau = 0$ where τ is the arrival time (Denzel et al. 2021). This means that images form at locations where τ has a minimum, a maximum, or a saddle point.

Equation 31 is evaluated for different positions of the image plane and the difference in the arrival time is calculated. This gives

$$\Delta t_{ij} = \frac{1+z_d}{c} \frac{D_s D_d}{D_{ds}} \left(\frac{1}{2} (\Theta_i - \beta)^2 - (\Theta_j - \beta)^2 - (\Psi(\Theta_i) - \Psi(\Theta_j)) \right), \quad (61)$$

where i and j correspond to the image positions for which the time delay is determined. The distances D_d, D_s and D_{ds} are calculated in angular diameter distances according to the formula

$$D_{AB} = \frac{1}{1+z_B} \int_A^B \frac{1}{a^2 H_0 \sqrt{\Omega_m a^3 + \Omega_{rad} a^4 + \Omega_\Lambda}}, \quad (62)$$

where A and B are the image positions. In calculating the angular diameter distances, a certain value of H_0 has already been assumed. To find an estimate for H_0 , it is excluded from Equation 62 and the distances are calculated as dimensionless quantities, i.e.

$$\tilde{D}_{AB} = \frac{1}{1+z_B} \int_A^B \frac{1}{a^2 c \sqrt{\Omega_m a^3 + \Omega_{rad} a^4 + \Omega_\Lambda}}. \quad (63)$$

Rearranging Equation 31 yields

$$H_0 = \frac{1+z_d}{\Delta t_{ij}} \frac{\tilde{D}_s \tilde{D}_d}{\tilde{D}_{ds}} \frac{1}{2} \left((\Theta_i - \beta)^2 - (\Theta_j - \beta)^2 - (\Psi(\Theta_i) - \Psi(\Theta_j)) \right). \quad (64)$$

Two different approaches are pursued. In the first approach, the time delays are computed for the image positions predicted by a reconstruction with 700, 1000, 1500 and 2000 Bessel roots. These time delays are compared to the predicted time delays using the total number of 2238 Bessel roots.

In the second approach, random noise with a standard deviation of 10 %, 1 % and 0.1 % of the mean coefficient value of the Fourier-Bessel series is added to all coefficients. The time delays are predicted using these noisy potentials and compared to the time delays predicted by the potential without including noise.

2.3.1 Code Structure

This section corresponds to the file `Timedelaypm.py`. To implement the formula for the time arrival surface, one must choose a specific point on the source plane, e.g. fix $\beta = 0$, where the source is placed. Using the same point mass distribution as in Section 2.2, the image plane is evaluated, and the arrival time surface is determined. For the readability of the image, the levels are defined to be separated by $\frac{t_{\max} - t_{\min}}{60}$.

Figure 12 shows the time arrival surface for the selected mass distribution. Small circles can be seen marking the positions where images will form. To confirm this, Figure 12 is compared with Figure 11. It can be seen that the images are formed at these positions. The imported gradients and the imported potential are both multiplied by a factor of 50 to enhance the image distances and make all features visible.

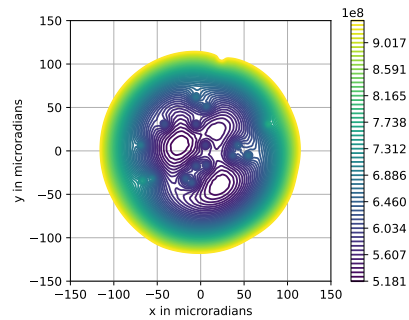
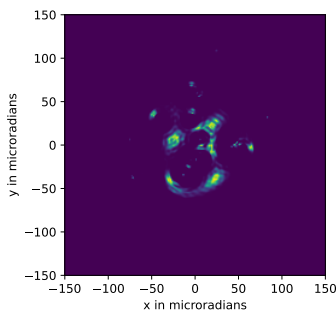


Figure 11: Images lensed by a point mass distribution Figure 12: Arrival time surface of lensed images

To numerically determine the time delay between different images of the same source, the time arrival contour is shown in Figure 12. The extrema are determined numerically and a specific pixel is obtained as the image position. The time differences can be evaluated at these determined points using Equation 61. This procedure is repeated for different redshifts.

To analyze those reconstructions, the obtained time delays are inserted into Equation 64. In a first approach, the time delays are determined for different numbers of Bessel roots. In a second approach, the time delays are calculated with noisy potentials. To determine these noisy potentials, random noise with a standard deviation of 10 %, 1 % and 0.1 % of the mean coefficient value is added to the Fourier-Bessel series coefficients. The time delays resulting from those noisy potentials are again inserted into Equation 64.

2.4 Large Cosmological Simulation of Mass Distribution

In a further step, realistic galaxy clusters are investigated. For this purpose, a large cosmological mass simulation originating from Stadel et al. 2022 is used as input data. The spatial scale of the simulation is 46.7 kpc per pixel. It contains 4000×4000 pixels, giving a total spatial scale of 187 Mpc \times 187 Mpc.

The simulation is not normalized, and before it is used for gravitational lensing, a normalization constant must be determined. For this simulation, the total density is assumed to be equal to the mean cosmological matter density.

In the Λ CDM model, the cosmology is described by six parameters. Table 1 shows the parameters found by the Planck Collaboration in 2016.

H_0	$67.48 \pm 0.98 \frac{\text{km}}{\text{sMpc}}$
$\Omega_b h^2$	0.02225 ± 0.00023
Ω_m	0.313 ± 0.013
τ	0.079 ± 0.019
$10^9 A_s e^{-2\tau}$	1.875 ± 0.014
n_s	0.9682 ± 0.0062

Table 1: Parameters of concordance cosmology (Planck collaboration 2016).

To determine the mean cosmological matter density, the parameter Ω_m is important. By definition

$$\Omega_m = \frac{\rho_m}{\rho_c}, \quad (65)$$

where ρ_c is the critical density. The critical density is the density at which the universe is flat. It has a value of $\rho_c = \frac{3H_0^2}{8\pi G} \approx 1.028613775 \cdot 10^{-26} \frac{\text{kg}}{\text{m}^3}$ using $G = 6.67408 \cdot 10^{-11} \text{ m}^3\text{kg}^{-1}\text{s}^{-2}$ (Merkatas et al. 2019) and $H_0 = 74.0 \pm 1.4 \text{ kms}^{-1}\text{Mpc}^{-1}$ (Riess et al. 2019). From Equation 65, a mean cosmological matter density of $\rho_m = 3.21956112 \cdot 10^{-27} \frac{\text{kg}}{\text{m}^3}$ is obtained.

The mean two-dimensional density of the simulated mass distribution must be scaled to be equal to the mean cosmological mass density. The mean cosmological mass density is three-dimensional, but by integration along the line of sight it becomes the projected two-dimensional density and can be compared to the density of the simulation. Therefore

$$\langle \Sigma_{\text{sim}} \rangle L^2 = \rho_m L^3, \quad (66)$$

where L is the total spatial scale of the simulation, i.e. 187 Mpc \cdot conv and $\langle \Sigma_{\text{sim}} \rangle$ is the average density of the simulation. The conversion from Mpc to m has a value of conv = $3.08567758128 \cdot 10^{22} \frac{\text{m}}{\text{Mpc}}$. Evaluating Equation 66 yields the average density of the simulation, i.e.

$$\langle \Sigma_{\text{sim}} \rangle = \rho_m \cdot L \cdot \text{conv}. \quad (67)$$

2.4.1 Code

This section corresponds to the file `Readh5.py`. The average density resulting from Equation 67 can be used to scale the values assigned to each pixel. The mass density on pixel p is determined by

$$\Sigma_{\text{sim}} = \frac{N_{\text{pix}} m_p}{\sum_q m_q} \times \langle \Sigma_{\text{sim}} \rangle, \quad (68)$$

where N_{pix} is the total number of pixels.

The Poisson equation is solved and the gradients of the potential are determined. Since the Poisson equation contains the convergence κ and not the two-dimensional density, the following relation is used for conversion

$$\kappa = \frac{\Sigma_{\text{sim}}}{\Sigma_{\text{crit}}}. \quad (69)$$

The original simulated mass distribution is already multiplied by the normalization constant, therefore only the inverse critical density factor is missing. Since the Poisson equation and the gradients are linear, the factor can be inserted before or after solving the Poisson equation and calculating the gradients of the potential.

In a last step, in the `GalaxyLensing.py` code and in the `Timedelay.py` code, $X_{\text{grad}}, Y_{\text{grad}}$ and the potential are multiplied by the factor $\frac{4\pi G D_d D_{ds}}{c^2 D_s}$ to find the real lensing effects and time arrival surfaces.

The entire mass distribution contains several galaxy clusters. In this work, two galaxy clusters are investigated. Individual galaxy clusters are therefore excluded from the large cosmological mass simulation. More specifically, a circular piece with a radius of 60 pixel is excluded from the overall simulation. A diameter of 120 pixels corresponds to a spatial scale of approximately 5.7 Mpc. A typical galaxy cluster has an extent on the order of megaparsecs. In the scope of this work, the Poisson equation is solved only for these particular regions of high density.

3 Results

In the following section, the reconstruction of the galaxy clusters is analyzed for different numbers of Bessel roots. In particular, the mass and potential error, the time delay and the image distances are determined for 700, 1000, 1500 and 2000 Bessel roots and compared to the overall reconstruction using all roots within $r_{\max} = 150$ microradians.

3.1 Reconstruction of Mass Distribution

Two circular pieces, each containing a cluster of galaxies are cropped out of the large-scale cosmological simulation. A total of 2238 Bessel roots are used to reconstruct the mass distributions. The simulated mass distributions and their reconstruction are shown in contour plots, see Figure 13.

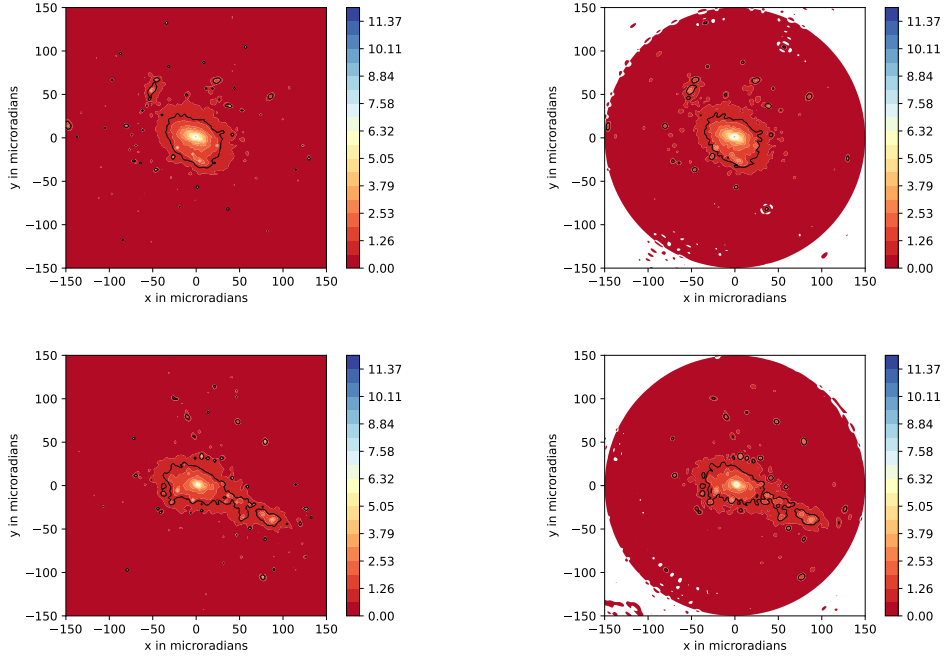


Figure 13: The projected simulated mass distribution (left) and mass reconstructions (right) for galaxy cluster 1 (top) and galaxy cluster 2 (bottom). The reconstructed mass distributions are normalized by the critical density $\Sigma_{\text{crit}} = 2.007 \frac{\text{kg}}{\text{m}^2}$. The black contour line marks the $\kappa = 1$ surface.

To show the convergence κ , the mass distribution of the galaxy cluster is normalized by the critical density, i.e. $\Sigma_{\text{crit}} = \frac{c^2}{4\pi G D_d} = 2.007 \frac{\text{kg}}{\text{m}^2}$ for a lens at redshift $z_l = 2$. The black contour shows the $\kappa = \frac{\Sigma}{\Sigma_{\text{crit},0}} = 1$ surface. Three-dimensional images of the simulated mass distributions and reconstructions as shown in Figure 13 are presented in Figure 14.

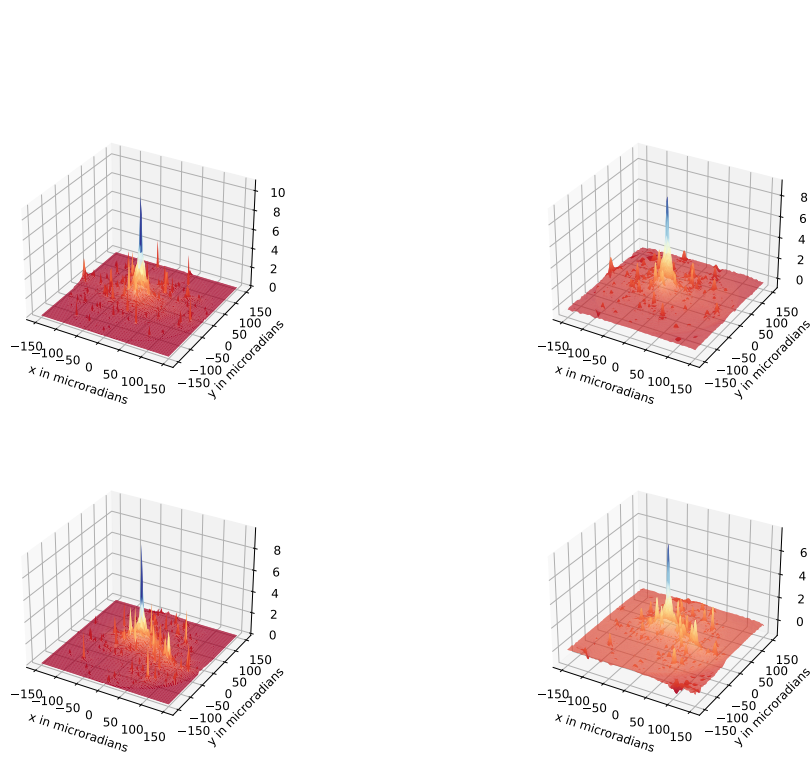


Figure 14: The simulated mass distribution (left) and mass reconstructions (right) for galaxy cluster 1 (top) and galaxy cluster 2 (bottom) plotted in 3D. The reconstructed mass distributions are normalized by the critical density $\Sigma_{\text{crit}} = 2.007 \frac{\text{kg}}{\text{m}^2}$.

The total mass error is defined as

$$\Delta m = m_{\text{simulation}} - m_{\text{reconstructed}}. \quad (70)$$

Illustrations of the total errors in the overall mass distribution of galaxy cluster 1 and galaxy cluster 2 are shown in Section A.1.1. The errors in the potentials are determined analogously, but since no reference potential is available, all potentials are compared to the final estimate with a maximum number of 2238 Bessel roots. The errors in the potentials are defined as

$$\Delta \Psi_i = \Psi_i - \Psi_{2238}, \quad (71)$$

where Ψ_i is the reconstructed potential with i Bessel roots. Images of the errors in the potentials are shown in Section A.1.3.

A quantitative overview is depicted in Figure 15 for galaxy cluster 1 and in Figure 16 for galaxy cluster 2. For the convergence κ and the potential Ψ_i , the mean and the root mean square (RMS) values are compared with the mean errors and the RMS of the corresponding errors.

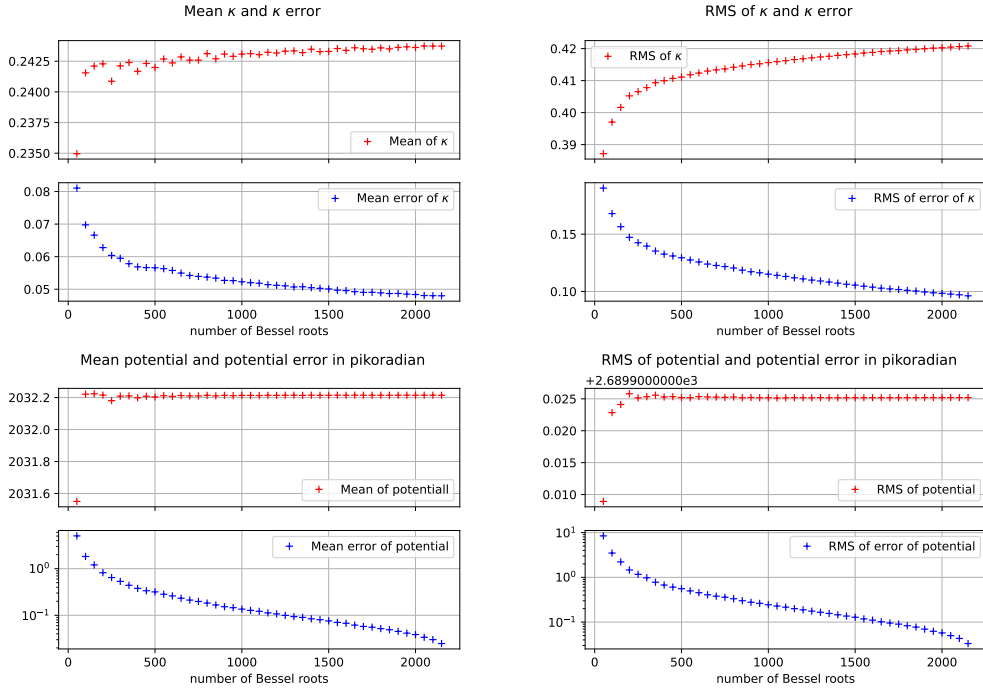


Figure 15: Error and RMS for the reconstruction of mass and potential for galaxy cluster 1.

For galaxy cluster 1, the mean κ for all pixels increases from $2.35 \cdot 10^{-1}$ for 50 Bessel roots to $2.44 \cdot 10^{-1}$ for 2238 Bessel roots. The error in κ decreases from $8.10 \cdot 10^{-2}$ for 50 Bessel roots to $4.80 \cdot 10^{-2}$ for 2238 Bessel roots. Comparing the initial mean error to the initial mean value of κ , the initial accuracy is 33.20 %. Comparing the final error in κ with the final mean value of κ , the final accuracy is 20.42 %. The corresponding RMS

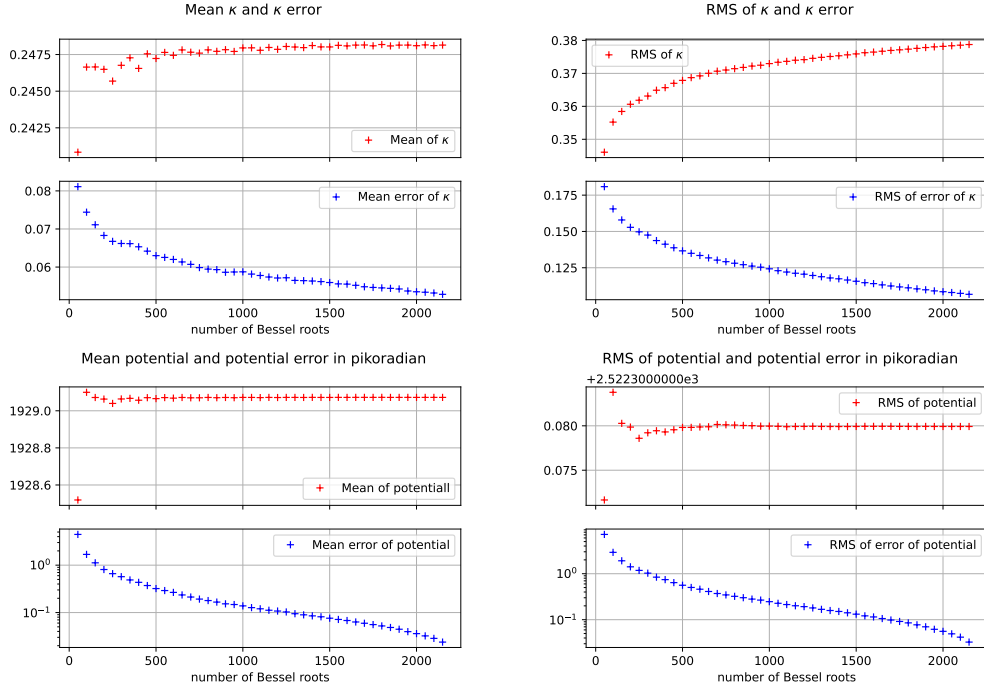


Figure 16: Error and RMS for the reconstruction of mass and potential for galaxy cluster 2.

values for κ are $3.87 \cdot 10^{-1}$ for 50 Bessel roots and $4.21 \cdot 10^{-1}$ for 2238 Bessel roots. The corresponding RMS values for the κ error are $1.90 \cdot 10^{-1}$ for 50 Bessel roots and $9.62 \cdot 10^{-2}$ for 2238 Bessel roots. These values correspond to 49.11 % and 22.87 %, respectively.

The mean value of the potential is $2.03 \cdot 10^3$ picoradians for 50 Bessel roots and $2.03 \cdot 10^3$ picoradians for 2238 Bessel roots. The corresponding errors are 5.05 picoradians for 50 Bessel roots and $2.48 \cdot 10^{-2}$ picoradians for 2238 Bessel roots. This corresponds to 0.25 % for 50 Bessel roots and 0.00122 % for 2238 Bessel roots. The RMS of the potential is $2.69 \cdot 10^3$ picoradians for 50 Bessel roots and $2.69 \cdot 10^3$ picoradians for 2238 Bessel roots. The RMS of the error of the potential is 8.45 picoradians for 50 Bessel roots and $3.31 \cdot 10^{-2}$ picoradians for 2238 Bessel roots. The corresponding accuracy is 0.407 % for 50 Bessel roots and 0.00159 % for 2238 Bessel roots.

For galaxy cluster 2, the mean κ value for all pixels increases from $2.41 \cdot 10^{-1}$ for 50 Bessel roots to $2.48 \cdot 10^{-1}$ for 2238 Bessel roots. The κ error decreases from $8.11 \cdot 10^{-2}$ to $5.28 \cdot 10^{-2}$. This corresponds to an initial accuracy of 33.68 % and a final accuracy of 21.29 %. The values for the RMS of κ are $3.46 \cdot 10^{-1}$ for 50 Bessel roots and $3.79 \cdot 10^{-1}$ for 2238 Bessel roots. The corresponding RMS values for the κ error are $1.81 \cdot 10^{-1}$ for 50 Bessel roots and $1.07 \cdot 10^{-1}$ for 2238 Bessel roots. These values correspond to the percentages 52.25 %, and 28.17 %.

The mean value of the potential is $1.93 \cdot 10^3$ picoradians for 50 Bessel roots and $1.93 \cdot 10^3$ picoradians for 2238 Bessel roots. The corresponding errors are

4.45 picoradians for 50 Bessel roots and $2.38 \cdot 10^{-2}$ picoradians for 2238 Bessel roots. This corresponds to 0.23 % and 0.00123 % for 2238 Bessel roots, respectively. The RMS of the potential is $2.52 \cdot 10^3$ picoradians for 50 Bessel roots and $2.52 \cdot 10^3$ picoradians for 2238 Bessel roots. The RMS of the error of the potential is 7.15 picoradians for 50 Bessel roots and $3.26 \cdot 10^{-2}$ picoradians for 2238 Bessel roots. The corresponding percentages are 0.367 % for 50 Bessel roots and 0.00167 % for 2238 Bessel roots, respectively.

The fractional mass difference is defined as:

$$\frac{\Delta m}{m} = \frac{m_{\text{simulation}} - m_{\text{reconstructed}}}{m_{\text{simulation}}} \quad (72)$$

Illustrations of the fractional errors of the total mass distribution of galaxy cluster 1 and galaxy cluster 2 are provided in Section A.1.2. The fractional mass error count for different numbers of Bessel roots is illustrated in Figure 17. With increasing number of Bessel roots, the high error regions become narrower.

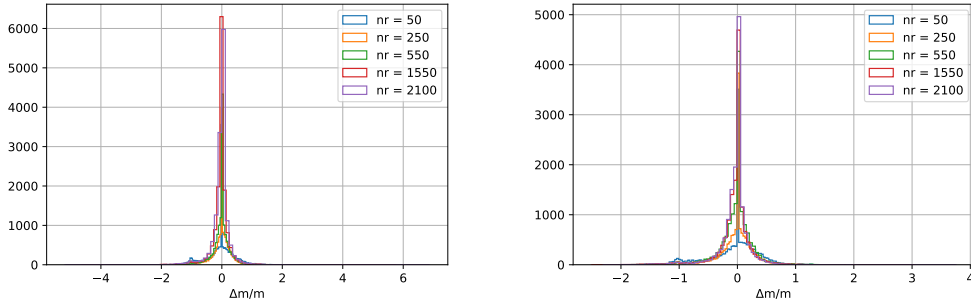


Figure 17: Fractional mass error count for a variety of Bessel roots for galaxy cluster 1 (left) and galaxy cluster 2 (right).

The input image contains $14'400$ pixels. Using the total number of Bessel roots, i.e. 2238 Bessel roots, $2238 \cdot 2 - 1 = 4475$ basis functions are available. For $m > 0$, two basis functions are used, one containing a sine and the other a cosine. For $m = 0$ the sine function vanishes and there is only one basis function left, hence the subtraction of 1. The maximal resolution of the reconstruction is therefore 0.31 basis functions per pixel. Another way to study the minimum scale of the reconstruction is to analyze the eigenvalues λ_{mn} . The λ_{mn} 's are wavelength which, when inverted and multiplied by 2π , give the minimum scale of the reconstruction. Their maximum value is $\lambda_{mn}^{max} = 1.00 \text{ microradians}^{-1}$, which gives a minimum scale of 6.28 microradians.

3.2 Gravitational Lensing of real Galaxies with reconstructed Clusters

After the reconstructed mass distributions of the galaxy clusters are found, they can be used to simulate gravitational lensing. In this section, only galaxy cluster 2 is considered. By analogy with Section 2.1.1, a Hubble Deep Field image is used. Other images of spiral galaxies are included as source images, as shown in Figure 18.



Figure 18: Galaxy 1 (NASA, ESA, and Heritage 2022), Galaxy 2 (NASA, ESA, and Hubble SM4 ERO Team 2022), Galaxy 3 (Hubble Heritage Team, ESA, and NASA 2020), Galaxy 4 (NASA, ESO, et al. 2019), Galaxy 5 (FORS, Antu, and ESO 2017), Galaxy 6 (NASA, ESA, W., et al. 2022)

A resolution of 2048×2048 is chosen for the Hubble Deep Field image. For the lensing of the individual galaxies, a finer resolution is chosen, i.e. $\text{res}_{\text{fine}} = \text{res} \cdot 5 \implies 10\,240 \times 10\,240$ pixels and only the central 20 microradians are analyzed, since all multiple images are located in this range. Another reason for choosing the central 20 microradians is the increased computation time of the code when a finer resolution is chosen. Fine resolution is necessary, because the pixels are enlarged when the images are magnified. When sources are lensed, it is common for them to be magnified.

The entire Hubble Deep Field image is placed at a redshift of $z = 9$ and the lensed images are calculated. The galaxies are located in positions of increasing redshift, namely $z_1 = 9.83$, $z_2 = 10.67$, $z_3 = 11.5$, $z_4 = 12.33$, $z_5 = 13.17$ and $z_6 = 14$. The lensed images are shown in Figure 19 and Figure 20. Two possible images are shown for each galaxy. These are sections of about 320×320 pixels to make the pixels visible, which corresponds to a scale of 46 microradians. The left image is lensed and shows the multiply imaged source, i.e. the lensed image. The right image shows the source without lens, so that the resolution of the measuring device, i.e. the pixelation can get observed.

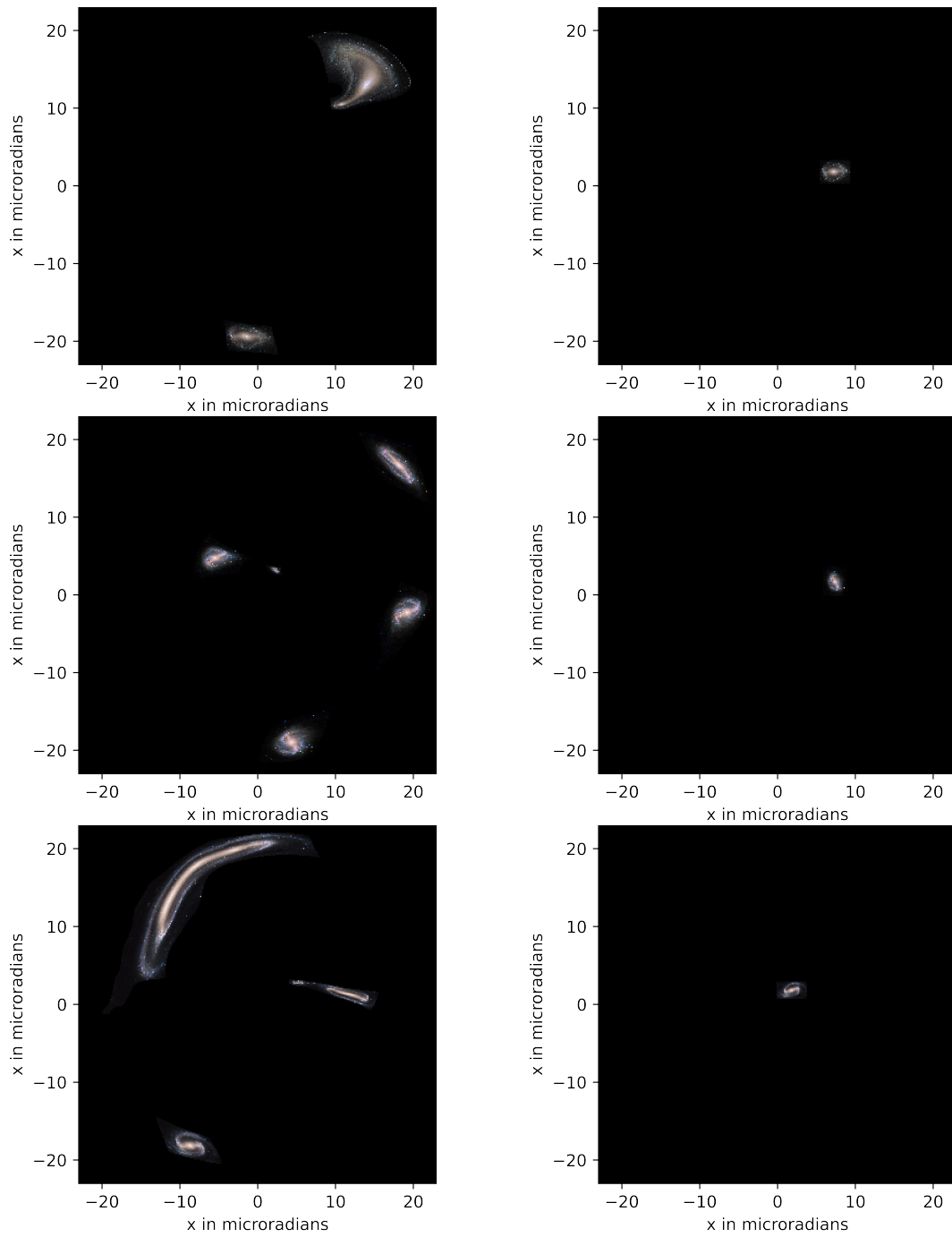


Figure 19: Images of the lensed (left) and unlensed (right) sources.

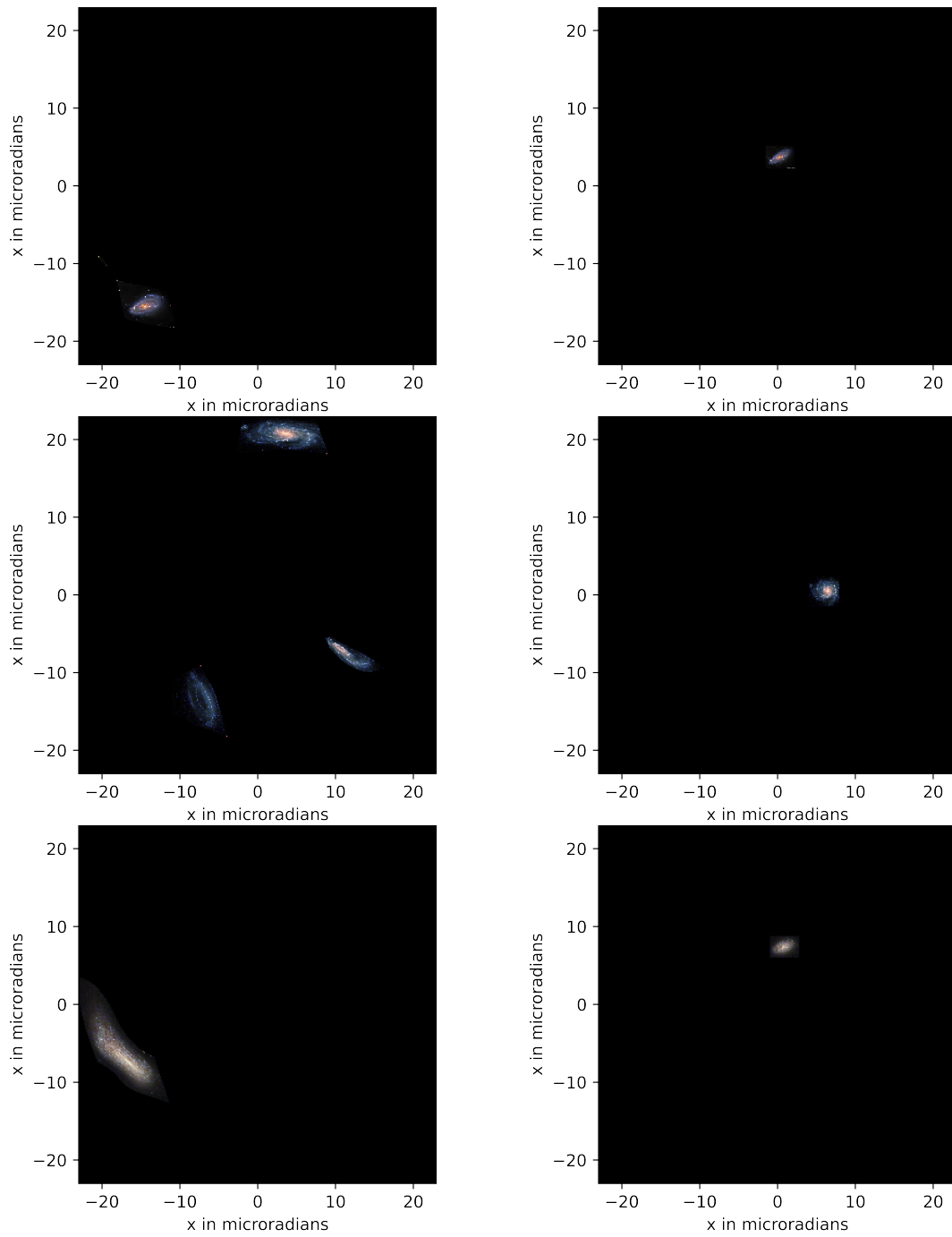


Figure 20: Images of the lensed (left) and unlensed (right) sources.

Finally, the lensed images of the galaxies and the Hubble Deep Field image are combined to produce a final simulation of a gravitationally lensed Hubble Deep Field, see Figure 21.

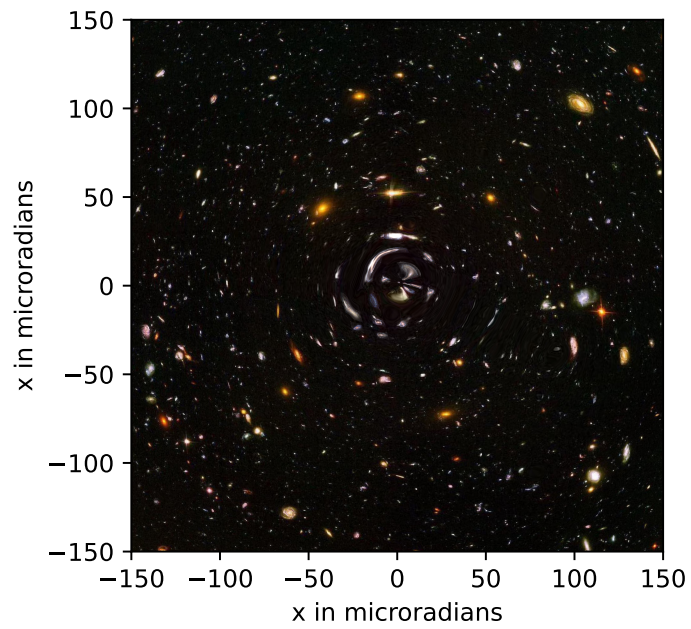


Figure 21: Lensed Hubble Deep Field with additional lensed spiral galaxies.

3.2.1 Time Delay and of Image Distances

In this section, the time delays and image distances of the images are analyzed for 700, 1000, 1500, 2000 and 2238 Bessel roots. A point source is constructed for $x_0 = 2$ and $y_0 = 2$ with an exponentially decaying brightness f , i.e.

$$f(X, Y) = \exp\left(-\frac{(X - x_0)^2 + (Y - y_0)^2}{5}\right). \quad (73)$$

A resolution of 2048×2048 pixels is chosen for the entire analysis. The maximum radius is again chosen to be $r_{\max} = 150$ microradians. The lensed images are constructed using the lens equation, see Equation 10. The time arrival surface is determined using Equation 31. This procedure is performed for various redshifts. The results are shown in Figure 22 for 700 Bessel roots, in Figure 23 for 1000 Bessel roots, in Figure 24 for 1500 Bessel roots, in Figure 25 for 2000 Bessel roots and in Figure 26 for 2238 Bessel roots. The color bar indicates the arrival time in seconds. The images occur at positions, where the time arrival surface has a minimum, a maximum or a saddle point. These points are determined numerically and are marked as red crosses in the figures. For the studied source and setup, five images can be observed in the image plane. Two of them are minima, one is a maximum and two are saddle points.

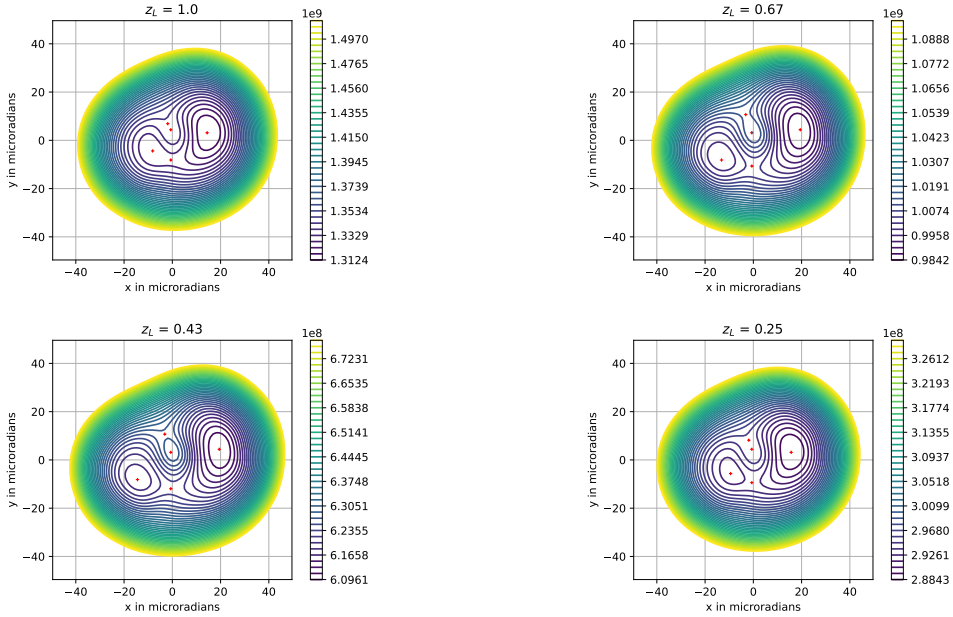


Figure 22: Time arrival surface (in seconds) for 700 Bessel roots. The minima, maxima and saddle points are marked with red crosses.

The distances in between the different image positions are determined for 2238 Bessel roots. All data for this section can be found in Section A.3. All image distances are in a range between 4.53 microradians and 36.14 microradians.

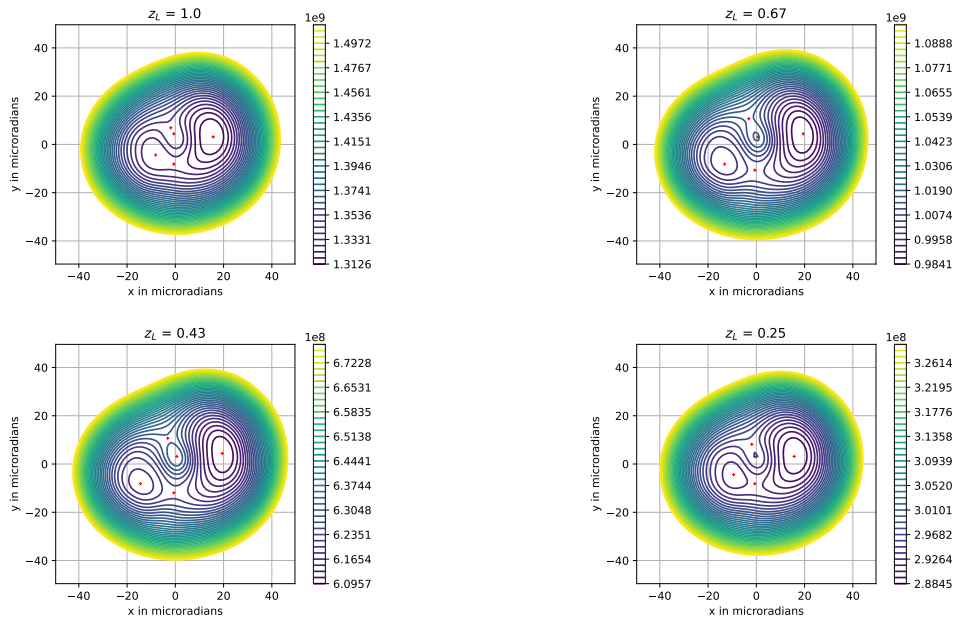


Figure 23: Time arrival surface (in seconds) for 1000 Bessel roots. The minima, maxima and saddle points are marked with red crosses.

The time delay in between images positions is determined after the image positions have been found. All time delays are listed in Section A.2.

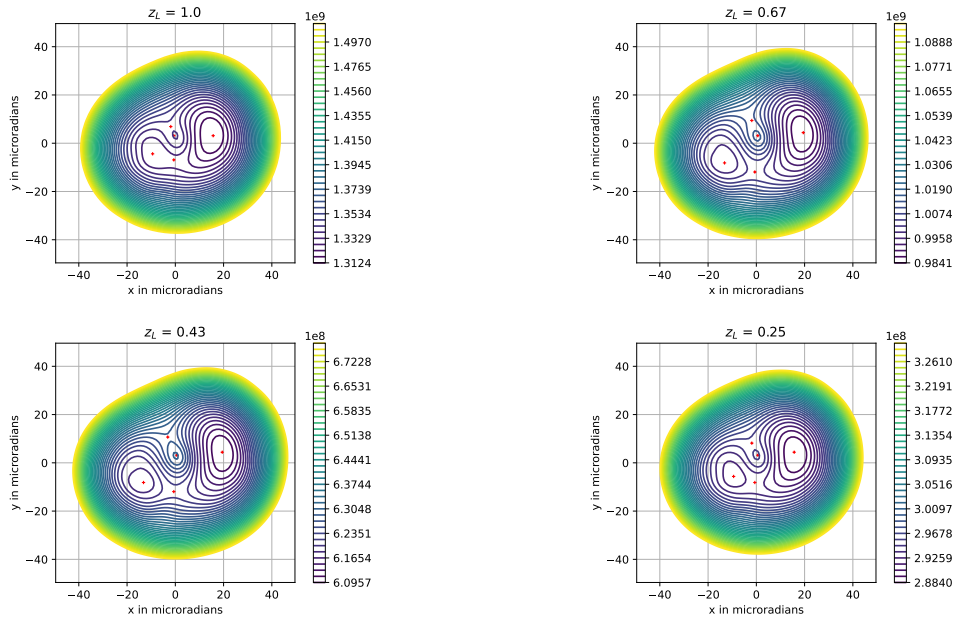


Figure 24: Time arrival surface (in seconds) for 1500 Bessel roots. The minima, maxima and saddle points are marked with red crosses.

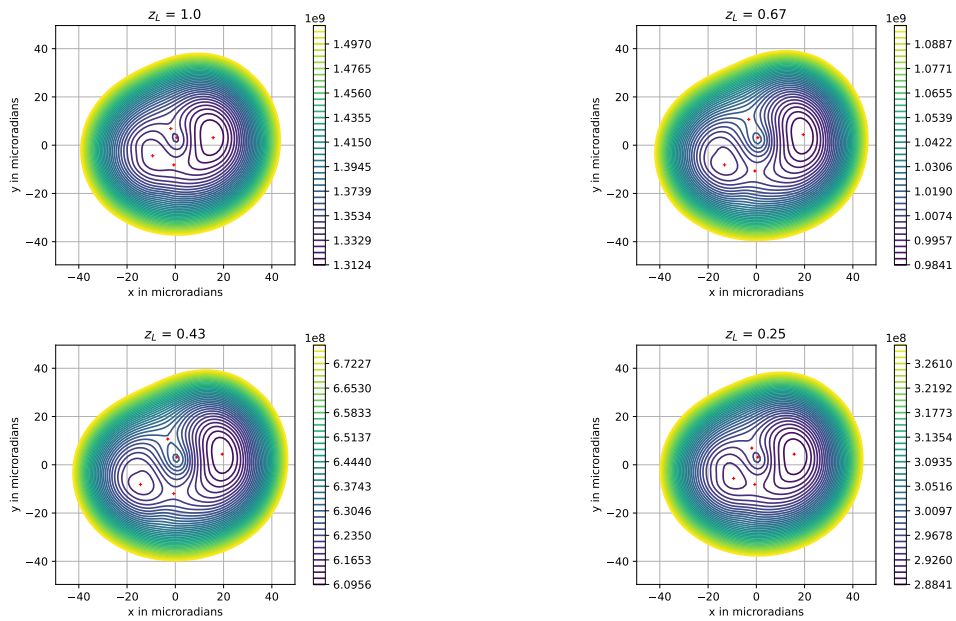


Figure 25: Time arrival surface (in seconds) for 2000 Bessel roots. The minima, maxima and saddle points are marked with red crosses.

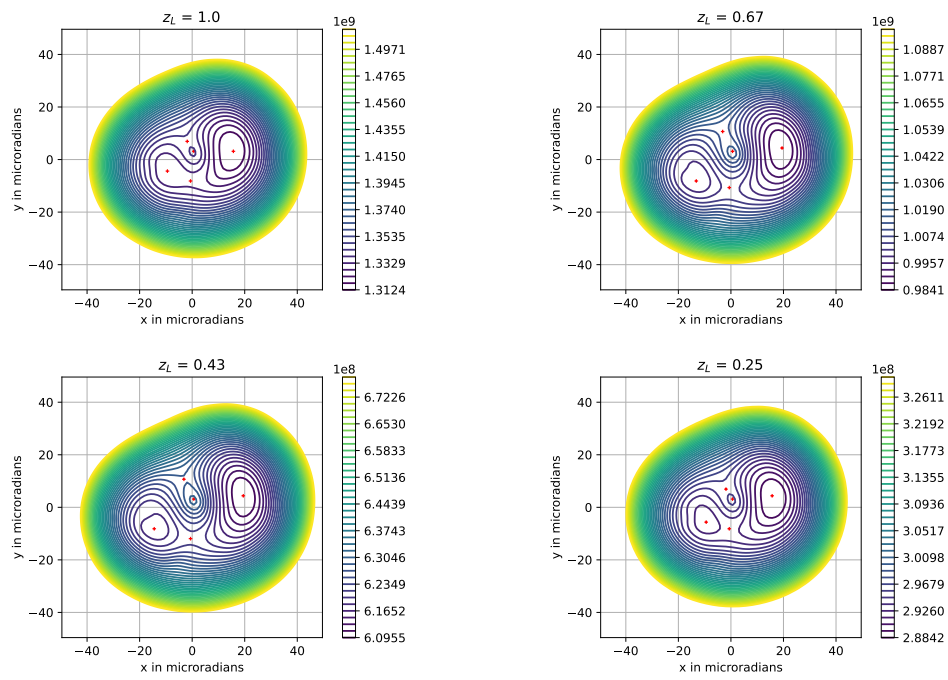


Figure 26: Time arrival surface (in seconds) for 2238 Bessel roots. The minima, maxima and saddle points are marked with red crosses.

The determined time delays for 700, 1000, 1500 and 2000 Bessel roots are compared in a next step with the reconstruction by using 2238 Bessel roots. Large errors occur mainly for close images, since the normalized error is larger for small differences in time delay. The median of the reconstruction with 700 Bessel roots is $M_{700} = 0.972$. 68% of the errors are contained in the interval between 0.924 and 1.007. This corresponds to an interval width of 8.33 %. The distribution of the normalized error in the time delay is shown in Figure 27. The median of the reconstruction with 1000 Bessel roots is

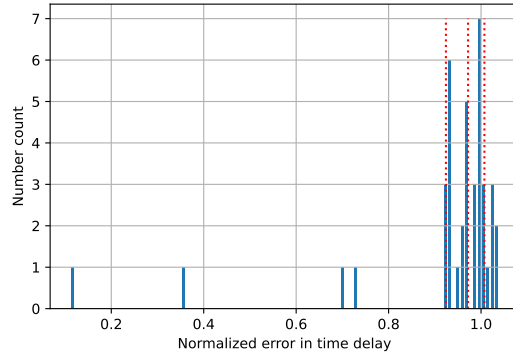


Figure 27: Normalized Hubble parameter 700 Bessel roots

$M_{1000} = 0.982$. 68 % of the errors lie in the interval between 0.950 and 1.000, which corresponds to an interval width of 5.05 %. The distribution is shown in Figure 28.

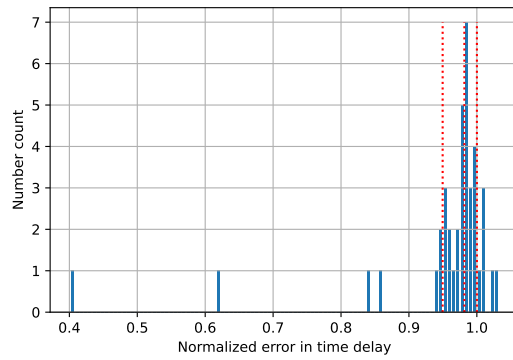


Figure 28: Normalized Hubble parameter 1000 Bessel roots

The median of the reconstruction with 1500 Bessel roots is $M_{1500} = 0.994$. 68% of the errors lie in the interval between 0.977 and 1.002, which corresponds to an interval width of 2.45 %. The distribution is shown in Figure 29.

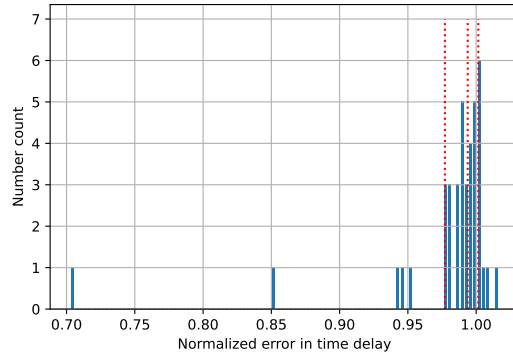


Figure 29: Normalized Hubble parameter 1500 Bessel roots

The median of the reconstruction with 2000 Bessel roots is $M_{2000} = 0.999$. 68 % of the errors lie in the interval between 0.995 and 1.001, which corresponds to an interval width of 0.56 %. The distribution is shown in Figure 30.

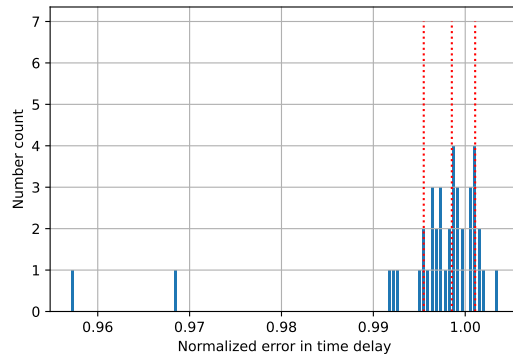


Figure 30: Normalized Hubble parameter 2000 Bessel roots

3.2.2 Estimation of the Hubble Parameter using a Noisy Potential

In this work, no direct measurements of time delays are included. To test the error-proneness of the reconstructed time delays, a different approach is taken. The time delay corresponding to a reconstruction with 2238 Bessel roots, determined in the previous section, is used as input data. Equation 64 is used to determine the Hubble parameter using the same image positions as used to calculate the time delays. Since the same procedure as before is performed, the output value is simply 1. In a next step, noise is added to the potential of the galaxy cluster. More specifically, random noise with a standard deviation of 10 %, 1 % and 0.1 % of the mean coefficient value is added to the Fourier-Bessel series coefficients. The mean value of the coefficients is 0.0148 and the median value is 0.0086. For each standard deviation, the potential is determined six times. Using the noisy potentials, the minima, maxima and saddle points of the time arrival surface are determined again. Three normalized distributions of H_0 are determined for the three noisy potentials.

Figure 31 shows the normalized distribution of the time delay for noise with a standard deviation of 10 % of the mean coefficient value. The distribution is centered around the median $M_{10} = 1.002$. 68 % of the values are contained in the interval between 0.993 and 1.019. This interval corresponds to a width of ≈ 2.63 %.

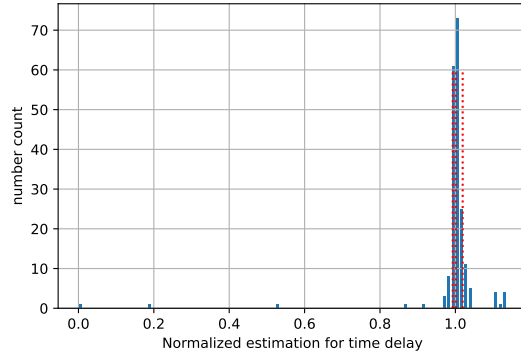


Figure 31: Estimation of the Hubble parameter for noise with $\sigma = 10$ %

Figure 32 shows the normalized distribution of the time delay for noise with a standard deviation of 1% of the mean coefficient value. The distribution is centered around the median $M_{100} = 1.003$. 68 % of the values are contained in the interval between 0.995 and 1.016. This interval corresponds to a width of ≈ 2.06 %.

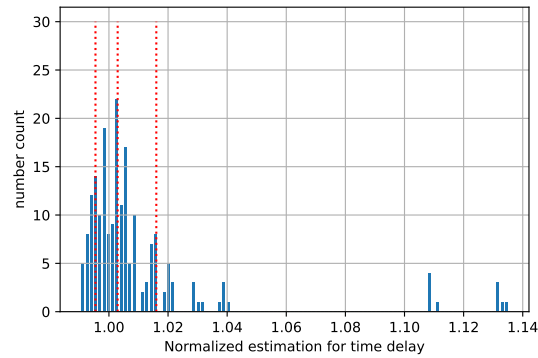


Figure 32: Estimation of the Hubble parameter for noise with $\sigma = 1\%$

Figure 33 shows the normalized distribution of the time delay for noise with a standard deviation of 0.1% of the mean coefficient value. The distribution is centered around the median $M_{1000} = 1.003$. 68 % of the values are contained in the interval between 0.996 and 1.015. This interval corresponds to a width of ≈ 1.95 %.

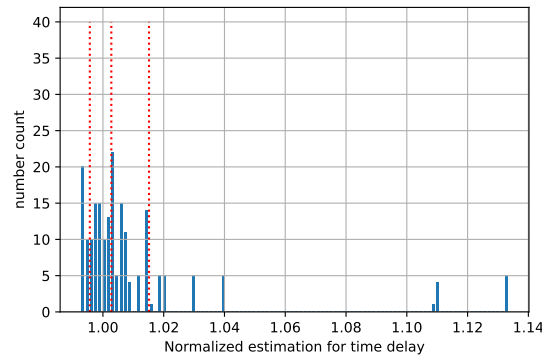


Figure 33: Estimation of the Hubble parameter for noise with $\sigma = 0.1\%$

4 Discussion

This work contains documentation of the development of a tool for simulating gravitational lensing. Random point mass distributions are reconstructed, time delays between different image positions are determined and lensed images are generated. The main result is the reconstruction of two galaxy clusters, which are cropped out from a simulation of a large-scale cosmological mass distribution. This reconstruction is performed using a Fourier-Bessel series approach. The series is oriented around the roots of the Bessel functions. By specifying a number of Bessel roots, the accuracy of the reconstruction is adjusted. An arbitrary accuracy can be chosen, and the corresponding number of Bessel roots can be determined from the analysis. For different numbers of Bessel roots, the reconstruction of the mass distributions, potentials, time delays and distances is investigated.

4.1 Reconstruction of Mass Distributions

The simulated mass distribution of galaxy cluster 1 and 2 and their reconstructions are shown in Figure 13. Three-dimensional plots of the same mass distributions are shown in Figure 14. The $\kappa = 1$ surface is marked with a black contour line. For galaxy cluster 1, a central peak and more or less uniformly distributed mass points around it can be seen. There is a small surplus of mass points in upper left corner of the image, but overall, the mass distribution is approximately spherically symmetric. During reconstruction, it can be observed that the general features of the mass distribution are captured. The central peak and multiple mass points in the outer region are captured. It can also be seen that there is a surplus of mass points in the upper left corner.

The mass distribution of galaxy cluster 2 is less symmetric than the mass distribution of galaxy cluster 1, showing an elliptically shaped central peak and a smaller peak in the lower right corner of the image. Some additional point masses are mainly located in the upper half of the image. The $\kappa = 1$ surface is again shown as a black contour line in the two-dimensional plot. In the reconstruction image, it be observed that the main features of the mass distribution are again captured, as the elliptically shaped central peak as well as the smaller peak in the lower right corner can be seen again. In contrast to the reconstruction of galaxy cluster 1, an underestimation of the mass contained in the cluster can be seen by eye. The $\kappa = 1$ surface is shifted towards the mass peaks. Additional mass is predicted outside the circular region containing the galaxy cluster.

The reconstruction of the mass distribution can be performed with any number of Bessel roots. To investigate the quality of the reconstruction, the mass error of the reconstruction is determined on each pixel of the distribution. This is done for a total of 42 reconstructions by increasing the number of Bessel roots by 50 roots in each step. The total and fractional mass errors for the reconstruction of the two galaxy clusters are shown in Section A.1.1 and Section A.1.2. The $\kappa = 1$ surfaces are again shown with a black contour.

For the total mass error, it is observed that the error shows an increasingly fine fingerprint pattern as the number of Bessel roots increases. Overall, the error decreases with increasing number of Bessel roots for both galaxies. The fractional mass error shows an

analogous finger print pattern, with additional maximum values around the smaller mass points and in the outer regions of the circle. A possible explanation for these features is that the mass in the non-central regions is very close to zero, so any small mass is a huge overestimation. The overestimation around the mass points can also be explained by the fact that the change in the mass distribution is very steep, which again is difficult to capture by reconstruction with smooth Fourier-Bessel functions.

In a next step, the total mass and the potential errors are examined. For each reconstruction corresponding to a given number of Bessel roots, the mean error and the RMS of the error of the reconstruction are calculated. The results are shown in Figure 15 for the reconstruction of galaxy cluster 1 and in Figure 16 for the reconstruction of galaxy cluster 2. For the reconstruction of galaxy cluster 1, the κ error decreases from 33.20 % to 20.42 %. The corresponding RMS error is 49.11 % for 50 Bessel roots and 22.87 % for 2238 Bessel roots. The fact that the RMS error is larger than the total error, indicates that there are large outliers in the reconstruction of the galaxy cluster. A possible explanation is the additional masses which are constructed outside of r_{\max} . The error in the potential is 0.25 % for 50 Bessel roots and 0.00122 % for 2238 Bessel roots. The corresponding values for the RMS are 0.407 % for 50 Bessel roots and 0.00159 % for 2238 Bessel roots. The error and RMS decrease by more than two orders of magnitude when the maximum number of Bessel roots is used. A possible explanation for this stronger minimization of the potential with respect to κ is that the potential is a smoother function. According to Gauss' divergence law, the gravitational potential outside any radius depends only on the total mass contained within that radius if the mass is radially symmetric (Forster 2017). Therefore, the potential in the outer regions does not depend on the specific positions of the constructed point masses inside, but only on the total mass contained in that radius. Both galaxies are approximately spherically symmetric, since the main mass is contained in a central circular peak.

Similarly, the errors in the reconstruction of galaxy cluster 2 are 33.68 % for 50 Bessel roots and 21.29 % for 2238 Bessel roots. The RMS values are 52.25 % and 28.17 %. The error of the potential is 0.23 % for 50 Bessel roots and 0.00123 % for 2238 Bessel roots. The RMS is 0.367 % for 50 Bessel roots and 0.00167 % for 2238 Bessel roots. Again, the error and RMS of the potential decrease more significantly, i.e. by two orders of magnitude, than the error and RMS and κ . The same argument applies as for galaxy cluster 1.

The reconstructed galaxy clusters are used for the simulation of strong gravitational lensing. For the lens equation, see Equation 10, only the gravitational potentials are required. An accurate reconstruction of the gravitational potential is therefore more important than the reconstruction of the mass distribution.

4.2 Gravitational Lensing of Real Galaxies with Reconstructed Clusters

The galaxy cluster 2 is used as a gravitational lens and lensed images are produced. Images of spiral galaxies are used as sources, see Figure 18. These images are placed at different redshifts. Two images are generated for each lens. One image shows an image of the source without lensing. The other image shows lensed images generated by the reconstructed galaxy cluster 2 as a gravitational lens. Comparing the two different images placed side by side in Figure 19 and 20, one can see the pixelation of the measuring device. The point spread function of the signal provides a maximum possible resolution, as only signals which are separated by more than the distance to the first minimum can be resolved. The pixel size of the device ideally corresponds to this resolution limit. If more pixels are available, no more information can be extracted from the system, but more useless data is generated. If fewer pixels are available, information is lost during the measurement process.

The superposition of the different lensing events corresponding to different redshifts is shown in Figure 21.

4.3 Time Delays and Image Distances of Complete Reconstruction

Currently, no gravitational lens with a redshift of $z = 6$ is listed in the Harvard Gravitational Lens Data Base. It is therefore not possible to compare the results with similar existing observations. Since the James Webb Space Telescope is right now in the process of observing and detecting new systems of gravitational lensing, new data will soon be available. Alternatively, the results obtained will be compared with various combinations of lens and source redshifts.

The system *RXJ0911 + 0551* is a quadruple quasar at $z = 2.80$, lensed by a cluster of galaxies at $z = 0.77$ (Hjorth et al. 2002). A time delay of 146 ± 8 days was measured. The the images distances are $\Theta_{AB} = 15.77$ microradians, $\Theta_{AC} = 14.9$ microradians, $\Theta_{AD} = 14.37$ microradians, $\Theta_{BC} = 2.31$ microradians, $\Theta_{BD} = 3.01$ microradians and $\Theta_{CD} = 4.65$ microradians.

The system *HE0435 – 1223* is located at $z = 1.689$ with a lens at $z = 0.454$ (Courbin, Chantry, et al. 2011). The measured time delays are 8.4 ± 2.1 days, 0.6 ± 2.3 days, 14.9 ± 2.1 days, 7.8 ± 0.8 days, 6.5 ± 0.7 days and 14.3 ± 0.8 days. The images distances are $\Theta_{AB} = 12.35$ microradians, $\Theta_{AC} = 7.7$ microradians, $\Theta_{AD} = 9.15$ microradians, $\Theta_{BC} = 7.34$ microradians, $\Theta_{BD} = 8.83$ microradians and $\Theta_{CD} = 10.83$ microradians.

Using different numbers of Bessel roots, galaxy cluster 2 is reconstructed. The minima, maxima and saddle points of the time arrival surface are determined numerically. The time arrival surface and the corresponding extrema as displayed in Figure 22 for 700 Bessel roots, in Figure 23 for 1000 Bessel roots, in Figure 24 for 1500 Bessel roots, in Figure 25 for 2000 Bessel roots and in Figure 26 for 2238 Bessel roots. The time delays predicted for the reconstructed cluster range from 5.31 days for $z_S = 0.25$ to 384.34 days for $z_S = 0.67$. The predicted minimal image distance is 5.53 microradians for $z_S = 1.00$ and $z_S = 0.25$. The predicted maximum image distance is 36.14 microradians for $z_S = 0.43$ microradians. The values are within the expected range.

To obtain an estimate of the error-proneness of time delays, the reconstructed time delays are compared with the time delays using the maximum number of 2238 Bessel roots. The width of the interval containing 68 % of the values is 8.33 % for 700 Bessel roots. The corresponding distribution is shown in Figure 27. For 1000 Bessel roots (see Figure 28), the width of the interval containing 68 % of the values is 5.05 %. For 1500 Bessel roots it decreases to 2.45 %, see Figure 29 and for 2000 Bessel roots to 0.56 %, see Figure 30. The error decreases approximately linearly.

In a second approach, the potential of the reconstructed galaxy clusters is perturbed to find some variation of the Hubble parameter. The galaxy clusters are reconstructed by a Fourier-Bessel series. The coefficients of the series are perturbed, by adding normally distributed random values. The random values are centered at 0 and have a standard deviation equal to 10 %, 1 % resp. 0.1 % of the mean coefficient value, respectively.

For noise with a standard deviation of 10 % of the mean coefficient value, the median is

1.002 and the standard deviation is 2.63 %, see Figure 31. For noise with a standard deviation of 1 % of the mean coefficient value, the predicted Hubble parameters have a median of 1.003 and standard deviation of 2.06 %, see Figure 32. For noise with a standard deviation of 0.1 % of the mean coefficient value, the median is 1.003 and the standard deviation of the predicted Hubble parameters is 1.95 %, see Figure 33.

Since all equations are linear, it would be expected that the standard deviation of the distribution of the time delays would be equal to the standard deviation of the noise. Comparing these three values shows that the time delay at 10 % does not have a scatter as large as would be expected based on the linearity of Equation 61. On the other hand, the standard deviation for noise corresponding to 0.1 % of the mean coefficient value has a larger scatter than expected.

An explanation for this could be that the mean value of the coefficients is 0.0148, while the median value is 0.0086. Thus, the median value is hence only 58.45 % of the mean. Hence, for most coefficients, the perturbation is greater than 10 %, 1 % and 0.1 % of their own value, respectively. This may explain the large standard deviation for 0.1 % noise.

Another important feature is that in the Fourier-Bessel series only few summands are catching the most important features. Those are weighted strongly and have correspondingly larger coefficients. The 10 % or 1 % of the mean coefficient value will have a relatively smaller error. This explains the lower standard deviation for 10 % and 1 %.

5 Conclusion

In the presented work, gravitational lensing is investigated as a tool to probe the model of the universe and. In a first step the lens equation is solved for an analytic potential. In a second step, an algorithm for approximation generic mass distribution with a Fourier-Bessel series is written. The main features of point mass distributions are captured. Additional noise is predicted in form of a fingerprint pattern. To find more realistic predictions for lensing events, it is favorable to consider realistic lenses. An analytic approximation is a suitable approach to determine the gravitational potential of a mass distribution and it is straightforward to calculate the lensing potential with it and this result can be inserted into the lens equation.

A simulation of a cosmological mass distribution is analyzed and two regions of high density are cropped out of the simulation. The diameter of the cropouts is in the order of 5 Mpc, a scale corresponding to galaxy clusters. Galaxy cluster 1 is an approximately spherically shaped cluster with a central peak, see Figure 13. Galaxy cluster 2 has a central peak and a smaller non-central second peak, also see Figure 13. Both galaxy clusters exceed the critical density, which means that there are regions with $\kappa > 1$. Thus, the condition for lensing to occur is fulfilled and multiple images are possible. Both clusters of galaxies are approximated with Fourier-Bessel series, varying the number of Bessel roots considered. As expected, the more roots considered, the more accurate the reconstruction becomes. Galaxy cluster 1 is reconstructed more successfully than galaxy cluster 2. A plausible explanation for this phenomenon is that galaxy cluster 1 is approximately spherically symmetric, a feature that is easier to catch using Bessel functions combined with sine and cosine functions, since more features are shared.

To simulate lensing events, only the reconstructed potentials are required. It can be seen that for both clusters of galaxies the RMS value of the potential error decreases by two orders of magnitude as the number of Bessel roots increases. The specific values for galaxy cluster 1 are 8.45 picoradians for 50 Bessel roots and $3.31 \cdot 10^{-2}$ picoradians for 2238 Bessel roots. The specific values for galaxy cluster 2 are 7.15 picoradians for 50 Bessel roots and $3.26 \cdot 10^{-2}$ picoradians for 2238 Bessel roots. In between, the RMS value of the error decreases monotonically, while the RMS value of the potential increases drastically at the beginning and takes a constant value afterwards.

Different spiral galaxies are used as source images to simulate gravitational lensing, using the reconstruction of galaxy cluster 2 as a gravitational lens. The lensing images are determined using the lens equation, assuming different redshifts of the lens and source. All resulting lensing images are overlaid with a Hubble Deep Field image that is also gravitationally lensed.

For each lensing event, the time delay between different observed image positions in the image plane is determined. The time delay is a sum of a geometrical and a gravitational time delay. For any given lens, the time arrival surface is determined and images can be seen to form at the specific positions where the time arrival surface has a minima, maxima or a saddle point. By numerically determining these minima, maxima and saddle points, the exact image positions are determined and the time delays are obtained.

The distances between the image positions range from 3.91 microradians to 26.70 microradians. For a reconstruction with the maximum number of Bessel roots, time delays are predicted in a range from 5.31 days to 384.34 days. The predicted time delays using 700, 1000, 1500 and 2000 Bessel roots are compared to the reconstruction corresponding to the maximum number. For 700 Bessel roots, the standard deviation of the distribution is 8.33 %. For 1000 Bessel roots it is 5.05%, for 1500 Bessel roots 2.45 % and for 2000 Bessel roots 0.56 %.

By inverting the equation for the time delay and using the fact that the angular diameter distances depend on the Hubble parameter of the current epoch, the Hubble parameter can be estimated.

The Hubble tension is still an issue in the recent Λ CDM model of the universe. The approach of using gravitational lensing to determine the Hubble parameter of the current epoch provides a completely independent strategy. With the James Webb Space telescope, new data becomes available and a huge potential is unlocked for which this tool can be helpful.

6 Acknowledgements

This project would not have been possible without my professor Prof. Dr. Prasenjit Saha. He not only offered me help and advice whenever I needed it, but also supported me in balancing my professional and personal life. I would like to especially thank Laura Rupp for her support during the work process. She always had an open ear and gave me great feedback. Special thanks also go to Ralf Gubler for his editorial help and encouragement during the project. I would like to thank David Degen for being a valuable companion during my studies and for his advice during this project.

References

- Andrews, G.E. (1999). *Special functions*, p. 199. DOI: 10.1017/CB09781107325937.
- Burke, W.L. (1981). “Multiple Gravitational Imaging by Distributed Masses”. In: *The Astrophysical Journal* 244, p. L1. DOI: 10.1086/183466.
- Courbin, F., V. Chantry, et al. (2011). “COSMOGRAIL: the COSmological MONitoring of GRAvItational Lenses. IX. Time delays, lens dynamics and baryonic fraction in HE 0435-1223”. In: *Astronomy and Astrophysics* 536.A53. DOI: 10.1051/0004-6361/201015709.
- Courbin, F. and D. Minniti (2002). *Gravitational lensing: An Astrophysical Tool*.
- Denzel, P. et al. (2021). “The Hubble constant from eight time-delay galaxy lenses”. In: *Monthly Notices of the Royal Astronomical Society* 000, pp. 1–12. DOI: 10.1093/mnras/staa3603.
- Di Valentino, E. et al. (2021). “In the realm of the Hubble tension — a review of solutions”. In: *Classical and Quantum Gravity* 38.15. DOI: 10.1088/1361-6382/ac086d.
- Dodelson, S. (2017). *Gravitational Lensing*, Chapter 2.
- Eddington, A.S. (1920). *Space, Time and Gravitation*. Vol. Cambridge.
- FORS, 8.2-meter VLT Antu, and ESO (2017). *Grand Spiral Galaxy NGC 1232*. URL: <https://apod.nasa.gov/apod/ap171226.html>.
- Forster, O. (2017). *Analysis 3*. 8th ed. DOI: 10.1086/682255.
- Giblin, B. et al. (2021). “KiDS-1000 catalogue: Weak gravitational lensing shear measurements”. In: *Astronomy and Astrophysics* 645.105. DOI: 10.1051/0004-6361/202038850.
- Guan, S., C.H. Lai, and G.W. Wei (2001). “Fourier–Bessel analysis of patterns in a circular domain”. In: *Physica D* 151, pp. 83–98. DOI: 10.1016/S0167-2789(01)00223-8.
- Hecht, E. (2016). *Optics*. Vol. Adelphi University. 5th edition, pp. 457–587.
- Hjorth, J. et al. (2002). “The Time Delay of the Quadruple Quasar RX J0911.4+0551”. In: *The Astrophysical Journal* 572, pp. L11–L14. DOI: 10.1086/341603.
- Hogg, D.W. (2000). “Distance measures in cosmology”. In: *Institute for Advanced Study, Princeton*. DOI: 10.48550/arXiv.astro-ph/9905116.
- Hubble Heritage Team, ESA, and NASA (2020). *Barred Spiral Galaxy NGC 1300*. URL: <https://apod.nasa.gov/apod/ap200611.html>.
- Lord Rayleigh (1888). “Wave theory of light”. In: *Encyclopædia Britannica* 24.91.
- Magnus, W., F. Oberhettinger, and R.P. Soni (1966). *Formulas and theorems for the special functions of mathematical physics*. Vol. Springer, p. 128. DOI: 10.1007/978-3-662-11761-3.
- Mercieca, K. (2016). *Light Vortex Astronomy*. URL: <https://www.lightvortexastronomy.com/how-to-very-accurately-calculate-your-telescopes-effective-focal-length.html>.
- Merkatas, C. et al. (2019). “Shades of Dark Uncertainty and Consensus Value for the Newtonian Constant of Gravitation”. In: *Metrologia* 5, p. 054001. DOI: 10.1088/1681-7575/ab3365.
- Miranda, M. (2007). “Gravitational lensing constraints on cosmic structures”. In: *Zurich Open Repository and Archive. University of Zurich*. DOI: 10.5167/uzh-163692.
- Mo, H., F. Van den Bosch, and S. White (2010). *Galaxy Formation and Evolution*, pp. 292–300. DOI: 10.1017/CB09780511807244.
- Mollerach, S. and E. Roulet (2002). *Gravitational Lensing and Microlensing*. Vol. ProQuest Ebook Central, pp. 7–68.
- Narayan, R. and M. Bartelmann (2008). *Lectures on Gravitational Lensing*. DOI: 10.48550/arXiv.astro-ph/9606001. URL: <https://arxiv.org/pdf/astro-ph/9606001.pdf>.

- NASA, ESA, and Hubble Heritage (2022). *Barred Spiral Galaxy NGC 1300*. URL: <https://apod.nasa.gov/apod/ap220508.html>.
- NASA, ESA, and the Hubble SM4 ERO Team (2022). *Barred Spiral Galaxy NGC 6217*. URL: <https://apod.nasa.gov/apod/ap220221.html>.
- NASA, ESA, Freedman W., et al. (2022). *Spiral Galaxy NGC 1512: The Inner Rings*. URL: <https://apod.nasa.gov/apod/ap220508.html>.
- NASA, ESO, et al. (2019). *M106: A Spiral Galaxy with a Strange Center*. URL: <https://apod.nasa.gov/apod/ap190317.html>.
- Planck collaboration (2016). “Planck 2015 results. XIII. Cosmological parameters”. In: *Astronomy and Astrophysics* 594.A13. DOI: 10.48550/arXiv.1502.01589.
- Refregier, A. (2021). “Lecture notes, part 2: Cosmological Background”. In: *ETH Zürich Astrophysics II*.
- Riess, A. et al. (2019). “Large Magellanic Cloud Cepheid Standards Provide a 1 percent Foundation for the Determination of the Hubble Constant and Stronger Evidence for Physics beyond Λ CDM”. In: *The Astrophysical Journal* 876.1. DOI: 10.3847/1538-4357/ab1422.
- Robertson, H.P. (1936). “Kinematics and world-structure III.” In: *The Astrophysical Journal* 83, p. 257.
- Schneider, P., J. Ehlers, and J. Falco (1992). *Gravitational Lenses*. DOI: 10.1086/682255.
- Schneider, P., C. Kochanek, and J. Wambsganss (2006). *Gravitational Lensing: Strong, Weak and Micro*. Vol. Swiss Society for Astrophysics and Astronomy. Saas-Fee Advanced Course 33, pp. 1–52.
- Subramanian, K. and S.A. Cowling (1986). “On local conditions for multiple imaging by bounded, smooth gravitational lenses”. In: *Monthly Notices of the Royal Astronomical Society* 219, pp. 333–346. DOI: 10.1093/mnras/219.2.333.
- Vera C., Rubin Observatory Project Mission Statement (2022). *Cosmic Shear*. URL: https://www.lsst.org/science/dark-energy/cosmic_shear.
- Whitney, H. (1995). “On Singularities of Mappings of Euclidean Spaces. I. Mappings of the Plane into the Plane”. In: *Annals of Mathematics* 62.3, pp. 374–410. DOI: 10.2307/1970070.
- Wucknitz, O. (2008). “From planes to spheres: about gravitational lens magnifications”. In: *Monthly Notices of the Royal Astronomy Society*, pp. 230–244. DOI: 10.1111/j.1365-2966.2008.13017.x.

A Appendix

A.1 Error in the Mass Distribution

A.1.1 Total Mass Error

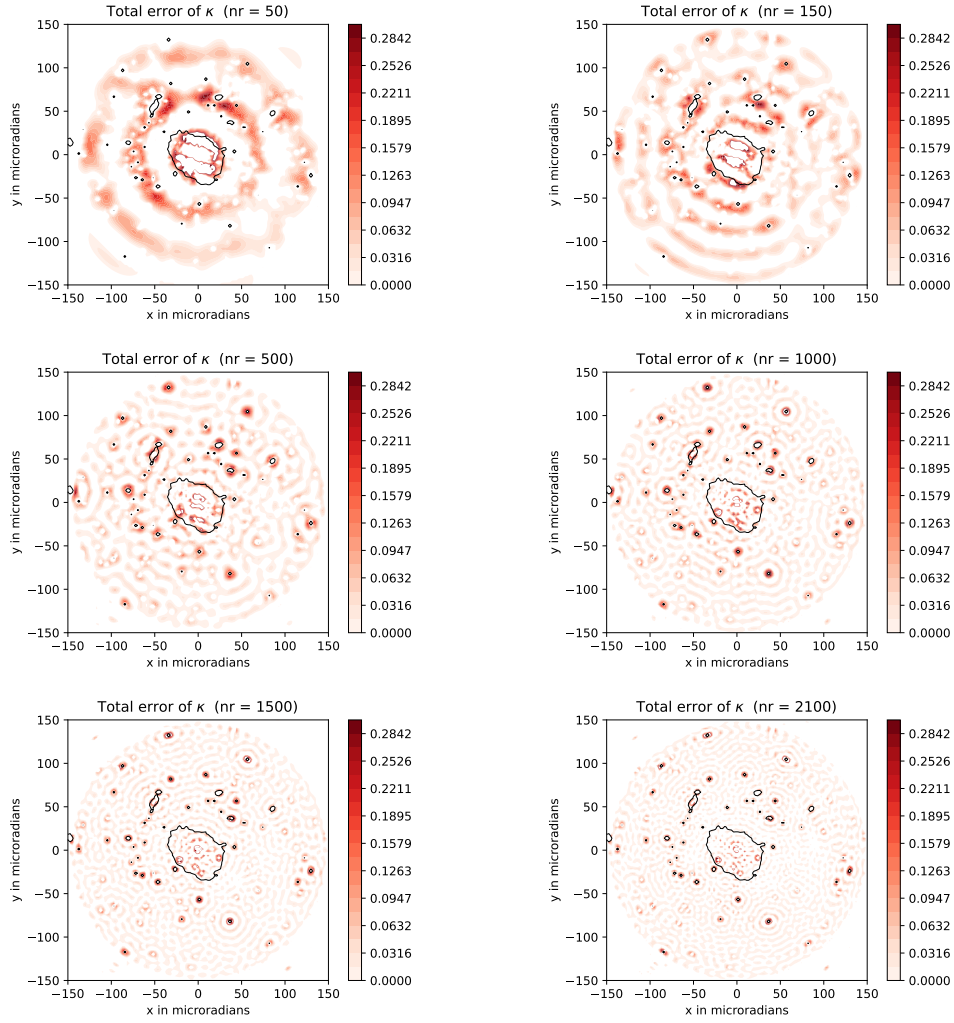


Figure 34: The total mass error of the reconstruction of galaxy cluster 1

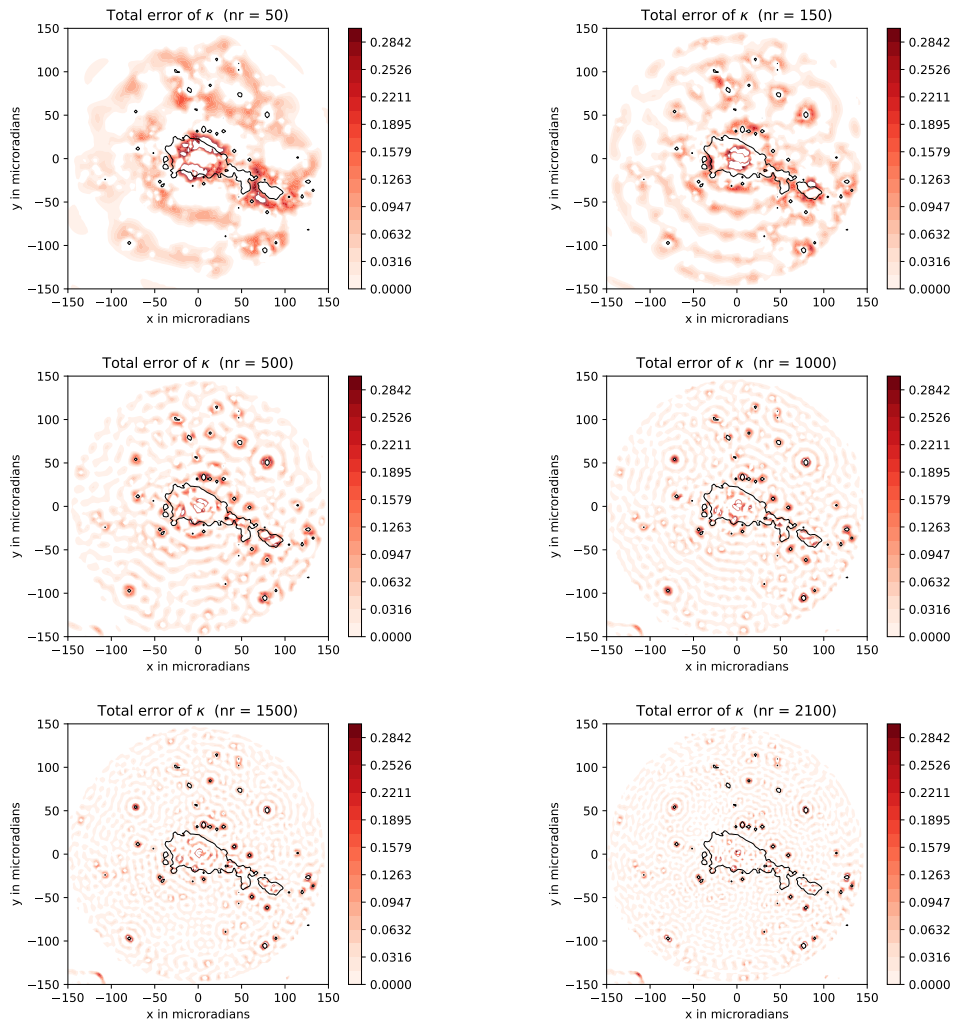


Figure 35: The total mass error of the reconstruction of galaxy cluster 2

A.1.2 Fractional Mass Error

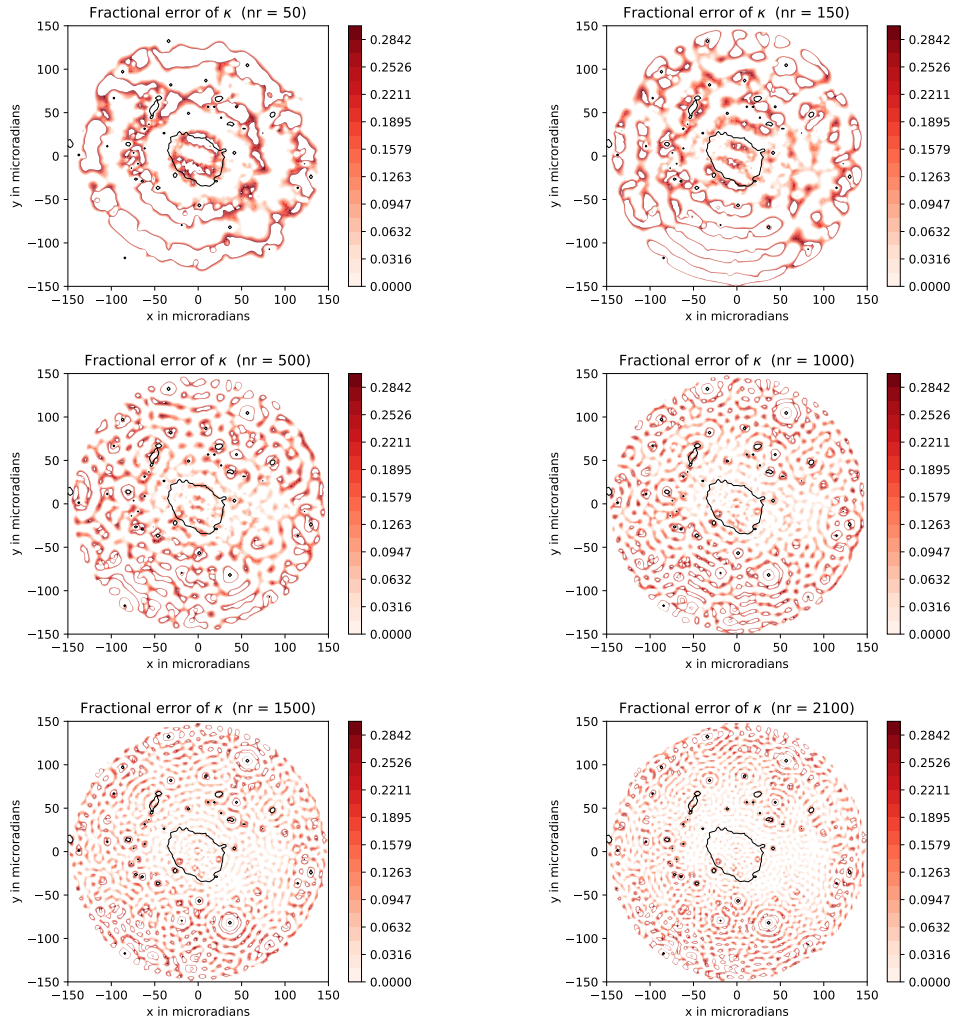


Figure 36: The fractional mass error of the reconstruction of galaxy cluster 1

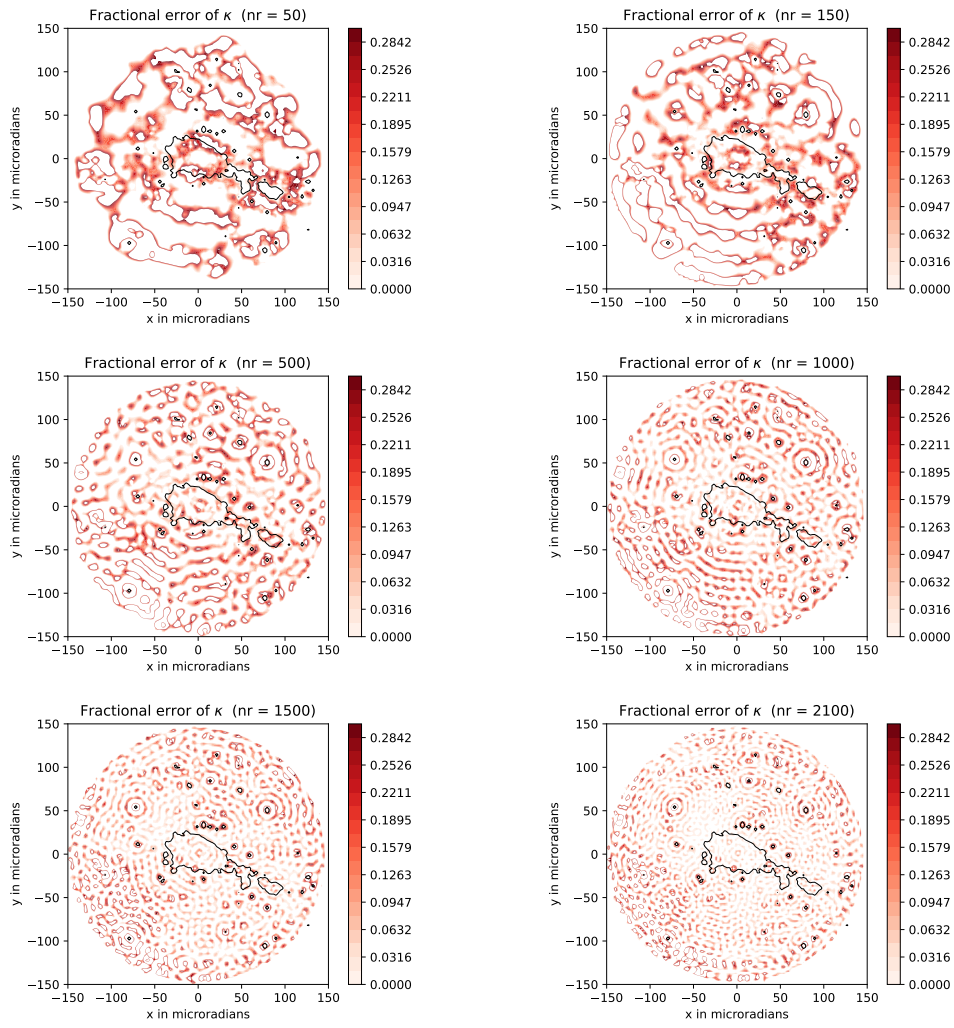


Figure 37: The fractional mass error of the reconstruction of galaxy cluster 2

A.1.3 Error in the Potential

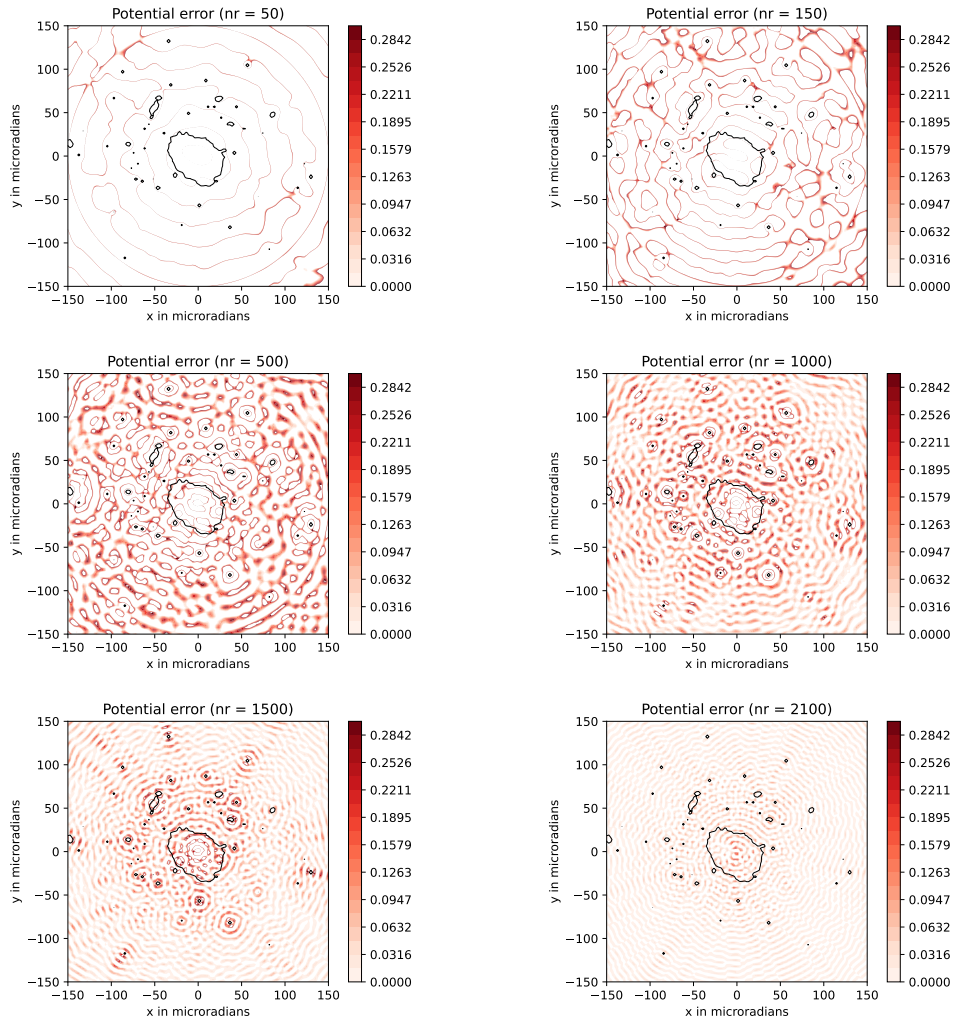


Figure 38: The potential error of the reconstruction of galaxy cluster 1

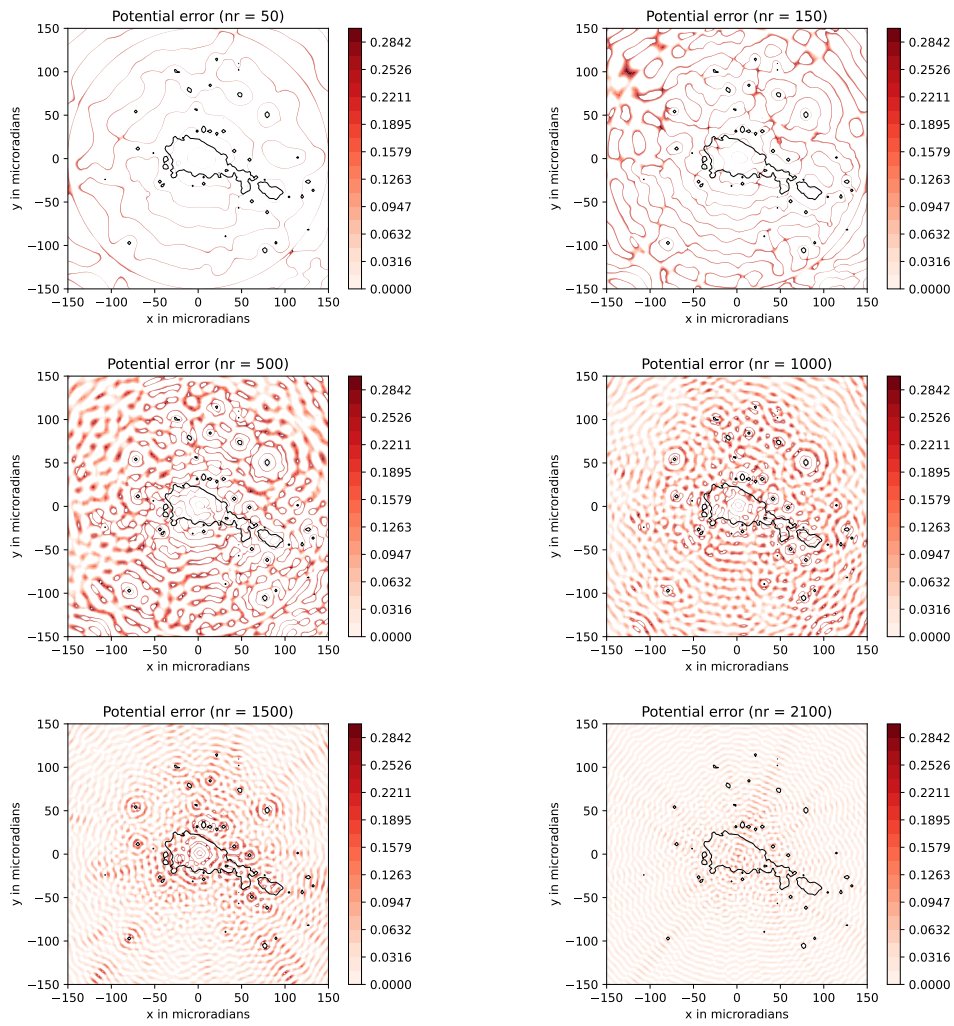


Figure 39: The potential error of the reconstruction of galaxy cluster 2

A.2 Time Delay

Lens Redshift	1.00	0.67	0.43	0.25
t_{AB} in days	17.688479	38.634001	26.866454	5.309040
t_{AC} in days	38.928795	71.132794	48.666734	11.068666
t_{AD} in days	126.225431	133.247931	85.334051	30.591842
t_{AE} in days	143.913910	141.329351	86.578610	35.900883
t_{BC} in days	165.154226	171.881932	112.200505	40.724032
t_{BD} in days	181.978339	204.380725	134.000786	41.660508
t_{BE} in days	182.842705	212.462146	135.245344	46.969548
t_{CD} in days	220.907134	243.014726	160.867240	51.792697
t_{CE} in days	347.132565	345.710077	220.579395	82.384539
t_{DE} in days	364.821043	384.344078	247.445850	87.693580

Table 2: The delay between image positions A,B,C,D and E for 2238 Bessel roots

Lens Redshift	1.00	0.67	0.43	0.25
t_{AB} in days	16.928669	38.311339	26.666338	5.141693
t_{AC} in days	38.631292	70.917397	48.447034	11.108782
t_{AD} in days	126.282292	132.908444	85.138426	30.604366
t_{AE} in days	143.210961	141.482061	86.744505	35.746059
t_{BC} in days	164.913584	171.219783	111.804764	40.753511
t_{BD} in days	181.842253	203.825841	133.585461	41.713148
t_{BE} in days	182.605847	212.399459	135.191540	46.854841
t_{CD} in days	221.237139	242.137180	160.251798	51.862293
t_{CE} in days	347.519431	345.307903	220.329966	82.466659
t_{DE} in days	364.448100	383.619241	246.996304	87.608352

Table 3: The delay between image positions A,B,C,D and E for 2000 Bessel roots

Lens Redshift	1.00	0.67	0.43	0.25
t_{AB} in days	12.434384	36.590360	25.290163	4.518744
t_{AC} in days	37.068574	71.816571	48.463902	10.958585
t_{AD} in days	128.294562	131.360733	84.710078	30.629235
t_{AE} in days	140.728946	140.997332	86.761950	35.147978
t_{BC} in days	165.363137	167.951093	110.000241	40.793503
t_{BD} in days	177.797520	203.177304	133.173980	41.587820
t_{BE} in days	183.132570	212.813903	135.225852	46.106563
t_{CD} in days	220.201144	239.767664	158.464143	51.752088
t_{CE} in days	348.495706	344.174636	219.935930	82.381323
t_{DE} in days	360.930090	380.764996	245.226093	86.900067

Table 4: The delay between image positions A,B,C,D and E for 1500 Bessel roots

Lens Redshift	1.00	0.67	0.43	0.25
t_{AB} in days	7.107244	32.447104	23.029324	3.270618
t_{AC} in days	38.290131	69.750267	47.964585	10.420014
t_{AD} in days	130.253987	130.778133	83.765194	30.842375
t_{AE} in days	137.361231	142.483270	87.176057	34.112993
t_{BC} in days	168.544118	163.225237	106.794518	40.727670
t_{BD} in days	175.651362	200.528399	131.729779	41.262389
t_{BE} in days	179.904103	212.233536	135.140642	44.533007
t_{CD} in days	218.194234	232.975503	154.759103	51.147684
t_{CE} in days	348.448221	343.011669	218.905836	81.990060
t_{DE} in days	355.555466	375.458773	241.935160	85.260677

Table 5: The delay between image positions A,B,C,D and E for 1000 Bessel roots

Lens Redshift	1.00	0.67	0.43	0.25
t_{AB} in days	1.980894	26.955936	19.475401	1.909074
t_{AC} in days	39.084482	65.335299	45.280064	10.750235
t_{AD} in days	130.997122	133.070589	84.953088	31.213764
t_{AE} in days	132.978017	144.631481	88.688623	33.122838
t_{BC} in days	170.081605	160.026525	104.428488	40.672066
t_{BD} in days	172.062499	198.405887	130.233151	41.963999
t_{BE} in days	181.047654	209.966780	133.968687	43.873073
t_{CD} in days	220.132137	225.361824	149.708552	51.422301
t_{CE} in days	351.129259	343.037368	218.921775	82.636065
t_{DE} in days	353.110153	369.993304	238.397175	84.545139

Table 6: The delay between image positions A,B,C,D and E for 700 Bessel roots

A.3 Image Distances

Lens redshift	1.00	0.67	0.43	0.25
$\Delta\Theta_{AB}$ in microradians	4.525797	8.420340	8.420340	4.525797
$\Delta\Theta_{AC}$ in microradians	9.559548	12.800886	14.311825	9.138213
$\Delta\Theta_{AD}$ in microradians	11.366592	13.864470	15.114972	11.366592
$\Delta\Theta_{AE}$ in microradians	12.552301	17.840172	18.828452	13.343279
$\Delta\Theta_{BC}$ in microradians	13.577390	18.870247	18.870247	14.638373
$\Delta\Theta_{BD}$ in microradians	15.062762	21.338912	21.957559	15.114972
$\Delta\Theta_{BE}$ in microradians	15.114972	21.486079	22.733184	15.114972
$\Delta\Theta_{CD}$ in microradians	17.972160	23.449634	23.449634	17.751635
$\Delta\Theta_{CE}$ in microradians	19.846931	25.104603	25.877232	20.587305
$\Delta\Theta_{DE}$ in microradians	26.209974	34.966665	36.141038	27.038484

Table 7: The angular image distances